BNL-225238-2024-JAAM

GRP-COEE-27

Single-phase local-high-concentration solid polymer electrolytes for lithium-metal batteries

W. Zhang, E. Hu

To be published in "Nature Energy"

February 2024

Chemistry Department

Brookhaven National Laboratory

U.S. Department of Energy

USDOE Office of Energy Efficiency and Renewable Energy (EERE), Office of Sustainable Transportation. Vehicle Technologies Office (VTO)

DISCLAIMER

Single-phase local-high-concentration solid polymer electrolytes for lithium metal batteries

Weiran Zhang[1], Volodymyr Koverga[2, 8], Sufu Liu[3], Jigang Zhou[4], Jian Wang[4], Panxing Bai[3], Sha Tan[5], Naveen Dandu[2, 8], Zeyi Wang[3], Fu Chen[6], Jiale Xia[3], Hongli Wan[3], Xiyue Zhang[3], Haochen Yang[3], Brett L. Lucht[7], Ai-Min Li[3], Xiao-Qing Yang[5], Enyuan Hu[5], Srinivasa R. Raghavan[3]*, Anh T. Ngo[2, 8]* & Chunsheng Wang[1, 3]*

[1]Department of Materials Science and Engineering, University of Maryland; College Park, MD 20740, USA.

[2]Materials Science Division, Argonne National Laboratory; Lemont, IL 60439, USA.

[3]Department of Chemical and Biomolecular Engineering, University of Maryland; College Park, MD 20740, USA.

[4]Canadian Light Source Inc., University of Saskatchewan; Saskatoon, SK S7N 2V3, CA.

[5]Chemistry Division, Brookhaven National Laboratory; Upton, NY 11973, USA.

[6]Department of Chemistry and Biochemistry, University of Maryland; College Park, MD 20742, USA.

[7]Department of Chemistry, University of Rhode Island; Kingston, RI 02881, USA.

[8]Department of Chemical Engineering, University of Illinois Chicago; Chicago, IL 60608, USA.

*Corresponding author. Email: cswang@umd.edu (C.W.); anhngo@uic.edu (A.N.); sraghava@umd.edu (S.R.)

Abstract: Solid polymers are promising electrolytes for Li metal batteries, but they have limitations: they cannot simultaneously achieve high ionic conductivity, mechanical strength, compatibility with the high-voltage cathodes, and the ability to suppress Li dendrites. Here, we design a class of local-high-concentration solid polymer electrolytes based on polymer blends, termed **L**i-**P**olymer in **F**-**D**iluter (LPIFD). The Li-polymer (polymer-in-salt) ensures continuous Li-ion conduction channels and contributes to solid electrolytes interphase (SEI), and the F-Diluter (inert fluorinated polymer) adds mechanical strength. Studies reveal that the single-phase LPIFD, based on a miscible polymer blend, lacks phase boundaries and forms an organic-less and LiF-rich SEI, effectively suppressing lithium dendrite. The single-phase LPIFD delivers ionic conductivity of 3.0 $x10^{-4}$ S cm^{-1}, and enables the Li anode to reach a high coulombic efficiency of 99.1% and a critical current density of 3.7 mA cm^{-2}. Furthermore, the ability to form F-rich cathode electrolyte interphase allows $LiNi_{0.8}Co_{0.1}Mn_{0.1}O_2$||Li cells to achieve a cycle life of 450 cycles at a high operating voltage of 4.5 V. This design will inspire efforts to commercialize polymer electrolytes for high-energy Li metal batteries.

Introduction

Lithium (Li) metal batteries are recognized as next-generation energy storage devices due to their high energy density and safety[1,2]. However, the growth of Li dendrites on Li anodes and the instability of high-voltage cathodes remain unresolved challenges, limiting their commercialization[3–6]. Since most electrolytes are not stable against Li metal anodes, a solid electrolyte interphase (SEI) on the Li anode is formed[7–9]. However, the SEI is not robust enough to suppress lithium dendrites[10,11], which reduces the Li plating/stripping coulombic efficiency (CE) and the cycle life of the cell.

Studies with liquid electrolytes have demonstrated that inorganic-rich (especially LiF-rich) SEIs can suppress Li dendrites. This is because LiF is highly lithiophobic (i.e., it has a weak affinity to Li). Therefore, Li migrates along the Li/SEI interface but Li dendrites do not grow through a LiF SEI[12–14]. In addition, LiF cathode electrolyte interphases (CEIs) have a high anodic stability of > 6.0V, enabling the use of high-voltage cathodes[15,16]. In liquid electrolytes, the reduction of fluorinated inorganic anions (such as PF_6^-, FSI^-) produces an inorganic lithiophobic LiF-rich SEI, while the reduction of organic solvents forms an organic/inorganic lithophilic SEI. To promote anion reduction and suppress solvent reduction, researchers have explored the use of high-concentration electrolytes (HCEs)[17–19]. To reduce the electrolyte viscosity while maintaining the same SEI composition, HCEs have been dissolved into fluorinated diluents to form localized high-concentration electrolytes (LHCE)[20–22]. On a different note, solid ceramic electrolytes have high mechanical strength and form inorganic SEI, which should be ideal for Li metal batteries[23,24]. However, the critical current density (CCD) of solid ceramic electrolytes is still limited, partly due to the inability to form LiF SEIs from the reduction of solid ceramic electrolytes. Additionally, the existence of grain boundaries promotes Li dendrite growth[25–27].

Solid polymer electrolytes (SPEs) can potentially combine the merits of liquid electrolytes (formation of LiF SEI and low interfacial resistance) and solid ceramic electrolytes (high mechanical strength). However, high CE values are rarely reported for SPEs in Li metal batteries[28,29], and most Li metal cells with SPEs have a low areal capacity[30] due to the low CCD. This is because the organic-rich SEIs formed in SPEs cannot suppress lithium dendrite growth (Fig. 1A). To form LiF-rich SEIs, a fluoroethylene carbonate (FEC) liquid solvent has been added to SPEs. However, the reduction of FEC also generated significant organic SEI. Therefore, the Li CE only reaches 97.6% with a CCD of 3.2mA cm^{-2}, which is still limited[20,31-32]. Similar to the HCEs, high-concentration polymer electrolytes (polymer-in-salt based on polyacrylonitrile, polyethylene oxide) have also been reported to form LiF-rich SEIs[33,34]. The high salt concentration and the solvent residues absorbed by the salt enhance the ionic conductivity. However, these also result in poor mechanical strength, thereby limiting their application in Li metal batteries (Fig. 1B). Researchers have attempted to enhance the mechanical strength of these electrolytes by adding an inert support matrix[35–38] or block copolymers[39]. For instance, Zhao et al. incorporated a combination of poly(ethylene carbonate) (PEC) and poly(vinylidene fluoride-co-hexafluoropropene) (PVDF-HFP) with a concentrated salt localized within the PEC[40]. However, these systems are typically phase-separated and inhomogeneous, which is unfavorable for achieving uniform Li deposition and SEI formation. Notably, Li dendrites can still grow along the phase boundaries[40–43] (Fig. 1C).

Herein, we demonstrate a new electrolyte based on a polymer blend, which we term Li-polymer in F-diluter (LPIFD). The single-phase LPIFD is a local-high-concentration polymer electrolyte formed by combining two miscible polymers: Li-polymer (polymer in salt) and F-diluter (inert fluorinated polymer) (Fig. 1D). The F-diluter, inert for Li-ion conduction, imparts high mechanical strength. Meanwhile, the Li-polymer with a high salt content provides high Li-

ion conduction and contributes to the formation of a LiF-rich SEI, effectively suppressing Li dendrite growth. Crucially, the high miscibility of the Li-polymer with the F-diluter eliminates phase boundaries, further enhancing the ability to suppress Li dendrites. As a result, the single-phase LPIFD exhibits both high mechanical strength and Li dendrite suppression capability.

As a concept demonstration, a fluorine-rich PVDF-HFP is selected as the inert F-diluter. PVDF and its corresponding polymer blends have been widely investigated for polymer electrolytes[44], but there is a notable gap in guidance for their design to attain high performance with Li anode. To illustrate the influences of phase boundary and SEI on the performance of LPIFD, we study a series of polymers [poly(propylene carbonate) (PPC); polyethylene oxide (PEO); poly(methyl methacrylate) (PMMA); poly(vinylsulfonyl fluoride) (PVSF); poly(bis(trifluoroethoxy)phosphazene] (PTFEP)] as Li-polymers, with lithium bis(fluorosulfonyl)imide (LiFSI) serving as the salt. Among these Li-polymers, PPC and PEO are not miscible with PVDF-HFP, resulting in phase-separated LPIFD[45,46] (Fig. 1C). PMMA is miscible with PVDF-HFP[47], but the reduction of an ester group gives rise to an organic-rich SEI, which reduces Li CE. The fluorination of polymers (PVSF and PTFEP) enhances their compatibility with the F-diluter[48]. Moreover, fluorination increases the F content and weakens the interaction with Li^+, promoting the formation of inorganic-rich fluorinated SEI. Consequently, the single-phase LPIFD electrolytes with inorganic-rich fluorinated SEI exhibit strong Li dendrite suppression ability, as indicated by a high Li plating/stripping CE of 99.1% and a CCD of 3.7 mA cm^{-2}. In addition, the single-phase LPIFD electrolyte forms an F-rich CEI, extending high voltage stability to 5.4V. This allows batteries to cycle at a cutoff voltage > 4.5 V, which is yet to be demonstrated[49]. Consequently, our electrolytes enable Li||$LiNi_{0.8}Co_{0.1}Mn_{0.1}O_2$ (NMC811) cells to reach a CE of 99.95% for 450 cycles at a cut-off voltage of 4.5 V, and a CE of 99.91% for over 200 cycles even at a cut-off voltage of 4.6 V. The exceptional performance of these cells is

attributed to (1) excellent Li dendrite suppression due to the formation of organic-less and LiF-rich SEI and the lack of phase-boundaries along with uniform Li deposition; (2) high-voltage stability due to the formation of a F-rich CEI; (3) enhanced ionic conductivity (3.0×10^{-4} S cm^{-1}) and mechanical strength. Additionally, the LPIFD concept for polymer electrolyte design is versatile and can be applied as an interlayer or binder for ceramic solid-state electrolytes, and also for micro-silicon anodes.

Design of LPIFD Electrolytes

We selected PVDF-HFP as the F-diluter because it has excellent mechanical properties and relatively high stability with lithium metal and high voltage cathodes[50–53]. We selected inorganic LiFSI as the salt because it is reduced to form a LiF-rich inorganic SEI on Li metal without organic by-products as in LiTFSI. The high content of LiFSI facilitates the formation of aggregated interconnective ionic clusters, promoting the formation of LiF SEI and providing percolation pathways for ion migration[33,54]. For the Li-polymer, we wanted a polymer that was miscible with the F-diluter, so that their mixture would form a single-phase LPIFD. We also wanted the polymer to have the capability to form LiF-rich SEI. With these considerations in mind, we investigated five polymers (Fig. 2).

The first two polymers, PPC and PEO, are non-miscible with PVDF-HFP, which forms phase-separated LPIFD. Between them, PEO demonstrates greater stability with lithium metal compared to PPC-LPIFD, because the decomposition of polycarbonate could result in higher organic composition in SEI while polyether is relatively stable at low potential. However, the phase separation significantly weakens the Li dendrite suppression ability. Among the three polymers that are miscible with PVDF-HFP, PMMA was found to form an organic-rich SEI, which

is not desirable. PVSF is an upgraded version of the PMMA. Even though the S=O on PVSF has a strong interaction with Li, which tends to be reduced, the almost inorganic nature promotes the formation of an organic-less SEI with LiF (reduction of S-F) in it. Furthermore, PTFEP is enriched with inorganic elements, and its weaker interaction with Li promotes the reduction of anion, allowing for an organic-less and LiF-rich SEI. To underscore the significance of developing a single-phase structure and an inorganic-rich fluorinated SEI, we choose three representative LPIFDs, based on PEO, PMMA, and PTFEP for detailed structure and properties characterization. To comprehensively illustrate the electrolyte design principle, the electrochemical performance of five LPIFD electrolytes was also compared.

The composition of the LPIFD was first optimized. To check the miscibility of PTFEP and PVDF-HFP, their blends were investigated by scanning electron microscopy (SEM), energy-dispersive X-ray spectroscopy (EDS) (Supplementary Fig. 1-3), and differential scanning calorimetry (DSC) (Supplementary Fig. 4). PTFEP is semi-crystalline[55] but has considerable backbone flexibility[56,57] and the strong electron-withdrawing ability of the trifluoromethyl group implies a weaker interaction of PTFEP with Li^{+}[58], which is promising for ionic conduction. At a PTFEP/PVDF-HFP weight ratio of 0.4, a homogeneous structure with continuous ionic conduction channels was formed, as can be seen from the uniform morphology in SEM and EDX, and the single glass transition temperature (T_g) in DSC (Supplementary Note 1). LiFSI was then added into the above polymer blend (Supplementary Note 2) until the salt content reached 63 wt%. The resulting electrolyte (denoted as PTFEP-LPIFD) has a low T_g of -63 ℃ (Supplementary Fig. 4C), and a high ionic conductivity 3.0 $x10^{-4}$ S cm^{-1} at room temperature with a low activation energy E_a of 0.18 eV (Supplementary Fig. 5). The high ionic conductivity is attributed to the high concentration of salt and the solvent absorbed by the salt.

For comparison, we prepared a PMMA-LPIFD and a PEO-LPIFD with the same composition ratio as the PTFEP-LPIFD. The precursor solutions of the three LPIFDs and images of the membranes are shown in Supplementary Fig. 6-7. The solvent residues remaining in the electrolytes are estimated by NMR (Supplementary Fig. 8) and we find that 16-19wt% 1,2-dimethoxyethane (DME) is present in all cases. These remaining solvents serve as a high-concentration plasticizer strongly bound with Li^+ ions that are localized to inert PVDF-HFP[59]. Although the solvent residue and high salt content can potentially weaken the mechanical properties of polymer electrolytes, all three LPIFDs still maintain strong solid-like rheology (Supplementary Fig. 9, with their storage modulus $G' >>$ their loss modulus G'') (Supplementary Note 3). Among the three, the PEO-LPIFD shows phase separation (Supplementary Fig. 10), with S elements (LiFSI) present more in the O-rich domain (PEO-rich) (Supplementary Fig. 11), consistent with the immiscibility of PEO and the PVDF-HFP. In contrast, PMMA-LPIFD and PTFEP-LPIFD exhibit a flat and uniform surface (Supplementary Fig. 12, 14) and uniform element mapping (Supplementary Fig. 13, 15) as expected from the miscibility of polymers. Moreover, the single-phase LPIFDs are very dense, lacking the distinct porous structure often observed in PVDF-based polymer electrolytes[44].

Structure and Properties of LPIFD Electrolytes

To understand the structure and chemistry of PEO-, PMMA- and PTFEP-LPIFD polymer electrolytes, a selected membrane region from each was characterized by scanning transmission X-ray microscopy (STXM) at the C, O, and F K-edges (Fig. 3). The different colors in Fig. 3A-C represent different regions on LPIFD electrolytes and their corresponding absorption information (Fig. 3D-F). The spectra for the PEO-LPIFD show the immiscibility between PEO and the PVDF-

HFP: note the distinct spectra in green and red regions (Fig. 3A, 3D, and Supplementary Fig. 16A and 16D). The red region is PEO-rich (in the C-edge spectra, the peak at 289.3 eV corresponds to the C-O bonds in PEO[60]), while the green region is rich in PVDF-HFP (the peak at 292.3 eV corresponds to the C-F resonance in PVDF-HFP[61]). In sharp contrast, both the PMMA- and PTFEP-LPIFD spectra show the miscibility of their constituent polymers (Fig. 3B, 3E, Supplementary Fig. 16B and 16E for the PMMA one, and Fig. 3C, 3F, and Supplementary Fig. 16C and 16F for the PTFEP one). Molecular dynamics (MD) simulations were conducted to complement the STXM observations at the atomistic level. The snapshots and the density profiles again confirm the poor miscibility of PEO with PVDF-HFP and a predominance of LiFSI in the PEO-rich region (Fig. 3G). In contrast, both PMMA and PTFEP are largely miscible with PVDF-HFP (Fig. 3H-I). This could be a result of the difference in the polarity of the polymers (Supplementary Fig. 17).

The STXM at the N, F K-edges (Supplementary Fig. 18-19) also reveal information about the extent of Li-FSI aggregation: this is higher in the PTFEP- LPIFD electrolyte than in the PEO- and PMMA-LPIFD electrolytes (Supplementary Note 4). This is attributed to the weaker interaction of PTFEP with Li^+ due to the electron-withdrawing -CF_3 group on the side chain, which has been quantitatively confirmed (Supplementary Fig. 20). Indeed, Li is prone to interact with more polar monomer fragments with highly negatively charged atomic sites, particularly -O- of PEO, O= and -O- of PMMA, and =N- and -O- in PTFEP. The coordination ability of Li···(O=)FSI calculated from the Li^+ local environment indicates strong Li-FSI interionic interactions inherent to LPIFDs (Supplementary Fig. 21) [22,62–64]. The high coordination ability of FSI and a high probability of Li-FSI aggregates (Supplementary Fig. 22-23) in LPIFD is attributed to the high concentration of Li salt and the presence of the fluorinated diluter.

The coordination environment of three LPIFD was characterized using oxygen K-edge X-ray absorption spectroscopy (XAS) before and after mixing with LiFSI salt (Fig. 3J). Upon mixing LiFSI salt into PEO/PVDF-HFP blends, the C-O peak at 532.08 eV shifts to higher energy due to the solvation of ethereal oxygen by Li^+[65]. Similarly, the C=O and C-O peaks in the PMMA/PVDF-HFP blend (at 531.1 eV and 531.9 eV) also shift to higher energy in the corresponding LPIFD[66]. A similar shift of the O peak at 532.0 eV in the PTFEP/PVDF-HFP blend is also observed in the corresponding LPIFD, suggesting that Li^+ solvation with O also occurs in this system. Moreover, the Fourier transform infrared (FTIR) spectroscopy (Fig. 3K, detailed analysis in Supplementary Note 5) proves the interaction of Li^+ with O and P=N in PTFEP. These interactions provide fast channels for Li^+ conduction, resulting in the high ionic conductivity of the LPIFDs. The weak interaction of Li^+ with PVDF-HFP was also confirmed (Fig. 3K).

The relative interaction strength between Li^+, FSI^-, and polymer can be inferred from the large peaks beyond 535eV (Fig. 3J), ascribed to S=O bonds[67,68]. As this molecular orbital is antibonding in nature, a higher energy level suggests a stronger interaction between Li^+ and FSI^-. This implies that in the PTFEP-LPIFD, the interaction between Li^+ and FSI^- is stronger, while the interaction between Li^+ and the polymer is weaker, promoting the reduction of anion to form an organic-less SEI. In addition, the XAS of the three LPIFDs before and after mixing with LiFSI salt were also calculated using density functional theory (DFT) (Supplementary Fig. 24). Good agreement with the experimental peaks was found (Supplementary Fig. 25).

In LPIFD electrolytes, the ionic conductivity, transference number, and mechanical strength are well correlated with the single-phase structure. In Supplementary Fig. 5, it is observed that PEO-LPIFD exhibits the lowest ionic conductivity and highest activation energy (E_a) among the three LPIFDs because the phase separation between PEO and PVDF-HFP blocks the ion-conductive channels. Conversely, the single-phase structures of the PMMA-LPIFD and the

PTFEP-LPIFD result in higher ionic conductivity. The latter has the highest conductivity, likely due to the weaker interaction of Li^+ and the corresponding higher solvent residue in that case. Turning now to the Li-ion transference number (t_{Li^+}), its values are 0.38 for the PEO-LPIFD (Supplementary Fig. 26A), 0.53 for PMMA-LPIFD (Supplementary Fig. 26B) and 0.64 for the PTFEP-LPIFD (Supplementary Fig. 26C), Again, the higher t_{Li^+} for the latter two is because of their single-phase structure, which ensures a homogeneous distribution of the Li salt. Note that the t_{Li^+} for the PTFEP-LPIFD surpasses typical SPEs[69]. The high t_{Li^+} facilitates efficient Li^+ transport, and it also helps to suppress Li dendrite by reducing the concentration gradient[70,71].

Next, regarding the mechanical properties, PEO is immiscible with PVDF-HFP, resulting in mechanically weaker PEO/PVDF-HFP blends compared to PVDF-HFP. In contrast, both PMMA and PTFEP are miscible with PVDF-HFP, enhancing the mechanical properties of PMMA/PVDF-HFP and PTFEP/PVDF-HFP blends over PVDF-HFP (Supplementary Fig. 27). As a result, even with a higher Li salt content, PTFEP-LPIFD is significantly stronger (modulus 23.3 MPa, Supplementary Fig. 28) and more thermally stable (Supplementary Fig. 29-30) than well-known PEO-based SPEs (Supplementary Note 6). This highlights the superiority of single-phase LPIFD design.

SEI Chemistry and Li anode Stability with LPIFD Electrolytes

The distinctive Li-polymer compositions of the three LPIFDs result in varied SEI chemistry. Figure 4 presents an X-ray photoelectron spectroscopy (XPS) analysis of SEI on Li anodes after cycling with three LPIFDs. As intended, LPIFD promotes the formation of LiF-rich SEI due to the high LiFSI salt concentration. Through the argon sputtering (depth profiling from top to bottom), a notable decrease in the ratio of carbon (organic species) in the SEI of PEO-LPIFD

is observed (Fig. 4A). This trend is also evident in the C 1s and O 1s spectra, where the C-C peak and Li_2CO_3 peaks decrease (Supplementary Fig. 31A), while the Li_2O peak gradually increases (Supplementary Fig. 32A), and LiF remains strong (Supplementary Fig. 33A). In contrast, the SEI formed in PMMA-LPIFD (Fig. 4B, and Supplementary Fig. 31B-34B) exhibits a considerably higher ratio of organic to inorganic components compared to that of PEO-LPIFD. This is attributed to the lower stability of the ester functional group of PMMA with Li metal than polyether, similar to liquid localized high-concentration carbonate electrolytes where the solvent decomposition leads to elevated carbon content in the SEI[15,72]. No C-F is detected in PEO-LPIFD and PMMA-LPIFD, while C-F is present in PTFEP-LPIFD (Supplementary Fig. 31C and 33C), indicating the inertness of PVDF-HFPand implying the non-uniform SEI formed in phase-separated LPIFD.

In contrast to the non-uniform SEI observed in PEO-LPIFD and the organic-rich SEI in PMMA-LPIFD, the atomic ratio of different elements in the SEI of PTFEP-LPIFD is almost constant from the surface to the inner SEI (Fig. 4C), and the peak intensities of different compositions are consistent at different depth (Supplementary Fig. 31C-34C). Moreover, relatively fewer C signals and higher F signals were detected in SEI, indicating an organic-less fluorinated SEI due to the high inorganic element ratio in PTFEP. In particular, a much stronger LiF peak was observed in the SEI of PTFEP-LPIFD (Supplementary Fig. 33C). The homogeneous LiF-rich SEI structure in PTFEP-LPIFD is attributed to the uniform distribution of PTFEP in the PVDF-HFP. LiF, being highly lithiophobic with weak bonding and high interfacial energy with Li metal, suffers less stress and retains strong mechanical strength during Li plating/stripping, promoting lateral deposition of metallic Li and suppressing the Li dendrite growth[73]. As a result, the homogeneous, organic-less, and LiF-rich SEI in PTFEP-LPIFD significantly contributes to Li dendrite suppression[20].

The distinctive structural features (with or without phase boundary) and SEI chemistry of the three LPIFDs result in the different Li dendrite suppression ability and Li plating/stripping CE. The Li dendrite suppression capability was evaluated by the critical current density (CCD) and cycling stability in symmetric Li||Li cells. In the case of PEO-LPIFD, short-circuiting was quickly observed at 0.6 mA cm^{-2} (Supplementary Fig. 35A). While PEO itself has high stability against Li metal and forms organic-less SEI due to the ether-based functional group, the phase-separation results in non-uniform Li deposition and SEI formation, allowing Li dendrite to grow along the phase boundaries of PEO and PVDF-HFP. PMMA is fully miscible with PVDF-HFP, forming a single-phase LPIFD. However, the ester-based functional group of PMMA forms an organic-rich SEI, promoting Li dendrite formation, especially at high current density. Therefore, short-circuiting is observed when the current density reaches 1.4 mA cm^{-2} (Supplementary Fig. 35B). In sharp contrast, PTFEP-LPIFD, with its single-phase structure and LiF-rich SEI, shows no short-circuiting until a high current of 3.7 mA cm^{-2} (Supplementary Fig. 35C). The Li||Li cell using PTFEP-LPIFD under an increasing current density from 0.5 to 8.5 mA cm^{-2} at a fixed capacity of 0.5 mAh cm^{-2} was also tested (Supplementary Fig. 36), indicating its potential for high current density applications. Figure 4D illustrates the cycling stability of Li||Li cells using the three LPIFDs at a current of 0.5 mA cm^{-2} for 1h charge/discharge, where PTFEP-LPIFD exhibits significantly longer cycling stability compared to PEO-LPIFD and PMMA-LPIFD, additional Li||Li test can be found in Supplementary Fig. 37.

To directly assess the effectiveness of Li dendrite suppression in single-phase structure and LiF-rich SEI, we examined the morphology of three LPIFD membranes after Li||Li cycling and identified Li dendrite inside the solid electrolytes using solid-state ^{7}Li NMR spectra with magic angle spinning[74–76]. The PEO-LPIFD sample revealed visible metallic Li on both the surface and inner regions (Supplementary Fig. 38A), indicating the growth of Li dendrites into the PEO-LPIFD

due to the presence of phase separations. In contrast, only a few dark spots, referred to as "dark lithium," were observed in single-phase PMMA-LPIFD and PTFEP-LPIFD (Supplementary Fig. 38B-C). The more pronounced decomposition in PMMA-LPIFD is attributed to the higher organic content in the SEI, in contrast to the PTFEP-LPIFD which forms a LiF-rich SEI and exhibits enhanced stability. In the NMR spectra of PEO-LPIFD, a prominent ^{7}Li NMR signal at 264 ppm (green star in Supplementary Fig. 39A) was observed in cycled PEO-LPIFD but absent in the fresh PEO-LPIFD, indicating significant lithium dendrite growth within the PEO-LPIFD. Conversely, only a weak peak corresponding to metallic lithium was observed in the amplified spectra of cycled PMMA-LPIFD and PTFEP-LPIFD (Supplementary Fig. 39B-C). The robust Li dendrite suppression capability from the single-phase structure and LiF-rich SEI is further supported by the bulky and smooth lithium morphology (Supplementary Fig. 40) as well as the cell electrochemical impedance (Supplementary Fig. 41) for PTFEP-LPIFD electrolytes after cycling (additional details in Supplementary Note 7).

The Cu||Li half cells were used to investigate the Li plating/stripping CE. The Li CE is mainly controlled by the single/separated phase and the SEI chemistry. As shown in Fig. 4E (red) and Supplementary Fig. 42A, the coulombic efficiency (CE) of PEO-LPIFD at a low current density of 0.3 mA cm^{-2} can quickly reach 98% due to the good stability of the ether group of PEO and organic-less SEI. However, phase separations lead to a quick short circuit (Supplementary Fig. 42A). The single-phase PMMA-LPIFD shows a much longer cycling stability (Supplementary Fig. 42B), but the Li CE could only reach 95% at the same current of 0.3 mA cm^{-2} after 300 cycles (Fig. 4E, pink). The low Li CE of PMMA-LPIFD is attributed to the organic-rich SEI generated by the reduction of the ester group in PMMA. When the current density was increased to 0.5 mA cm^{-2}, the cell short within 100 cycles, and Li CE was further reduced (Supplementary Fig. 43). In sharp contrast, even at a current density of 0.5 mA cm^{-2}, the Li||Cu half-cell using PTFEP-LPIFD

can reach a high CE ~99.1% after 300 cycles (Fig. 4E, blue; for more CE test see also Supplementary Fig. 44), a long cycle with stable voltage polarization is also observed (Fig. 4F).

The morphology of Li metal deposited on Cu was also investigated. At a current density of 0.3mA cm^{-2} and a capacity of 0.6mAh cm^{-2}, the top view of the deposited Li shows a nodule-like structure rather than a whisker-like dendrite structure (Fig. 5A and 5B), which agrees with the organic-less SEI in PEO-LPIFD. However, phase separation between Li-PEO and F-diluter results in non-uniform Li plating. Cross-section images of deposited Li show a thickness of 9.2μm with a non-uniform structure and numerous holes (Fig. 5C). As for PMMA-LPIFD, the morphology of deposited lithium exhibits a whiskers structure (Fig. 5D and 5E) which is consistent with its low CE of 90%. The cross-sectional images of Li after plating of 1.0 mAh cm^{-2} displayed a thickness of 9.0μm with a loosely packed structure (Fig. 5F). In sharp contrast, the Li after plating for 2.0 mAh cm^{-2} using PTFEP-LPIFD exhibited a very dense surface with a compact structure and a thickness of 10.1 um (Fig. 5G-I). This chunky Li is deposited with low tortuosity and intimate connection to maintain the bulk integrity as the robust LiF-rich SEI prevents the deposited Li from dendrite growth [57,77,78].

To comprehensively demonstrate the design criteria (aiming for a single-phase structure and LiF-rich SEI), we conducted tests with additional polymers as shown in Fig. 2, summarized in the table of Fig. 5J. Similar to PEO, PPC is immiscible with PVDF-HFP, resulting in a phase-separated PPC-LPIFD (Supplementary Fig. 45). In addition, the reduction of polycarbonate forms an organic-rich SEI compared to PEO-LPIFD. As a result, the PPC-LPIFD has the lowest CCD (0.3 mA cm^{-2}) and CE (<90%) (Supplementary Fig. 45) among these polymer blends. In contrast, PVSF is miscible with PVDF-HFP. An almost inorganic structure contributes to an organic-less SEI. Therefore, PVSF achieves both higher CE (99%) and CCD (2.4mA cm^{-2}) (Supplementary Fig. 46). Overall, the formation of a LiF-rich and organic-less SEI with a single-phase structure

underscores the excellent stability of LPIFD with Li and its superior lithium dendrite suppression ability.

Performance of Li//NMC811 Full Cells at High Voltage

Similar to the liquid localized high-concentration electrolyte, a high concentration of LiFSI and a high ratio of F in LPIFD enables LPIFD to achieve high anodic stability, supporting the high voltage cathode (NMC811). As shown in Fig. 6A, the PTFEP-LPIFD exhibits anodic decomposition of above 4.9 V, which is further enhanced to 5.4V after two passivation cycles[79,80]. It is noteworthy that the utilization of solid polymer electrolytes with high-voltage cathodes has traditionally been limited to a voltage of 4.3V[79,80].

The electrochemical behavior of NMC811 using PTFEP-LPIFD was evaluated in Li||NMC811 coin cells with excess Li and an aggressive cut-off voltage of 2.8 - 4.5V. The NMC811 cathode's areal capacity is around 1-1.3 mAh cm^{-2}. As shown in Fig. 6B and 6C, the NMC811in PTFEP-LPIFD delivers a very high initial CE of 93.95%, and the CE quickly reaches >99.9% within 5 cycles, indicating that a robust CEI was quickly formed on the NMC811 surface with minimal capacity loss during the CEI formation. Moreover, the cell presents a superior cycle life of >400 cycles (80% retention) at 0.5C with a high average CE of 99.95% (Fig. 6C), and a minor average voltage decay (Fig. 6D), indicating excellent stability at high voltage. To verify the scalability, a pouch cell was assembled using NMC811 and 20um Li foil (N/P 4.3) with PTFEP-LPIFD electrolyte (Fig. 6E). After five pre-cycles, there is no obvious capacity fading over 100 cycles at 0.3C, and the average CE remained high at 99.945%, consistent with the good performance observed in coin cells with thin Li (Supplementary Fig. 47-48).

Fast charging of batteries is crucial for electric vehicle applications, but it remains an unresolved challenge. Achieving fast charging in a Li||NMC811 battery with solid polymer electrolytes is particularly challenging due to larger overpotential and poorer contacts compared to liquid electrolytes. Therefore, the high voltage stability of the solid polymer electrolytes is extremely important for fast charging because a high cut-off charging voltage can offset the large overpotential at high current density, thereby mitigating capacity loss attributed to overpotential. Here, the PTFEP-LPIFD demonstrates remarkable stability at a high voltage of 4.6V, reflected by a high-capacity retention of 79.7% after 200 cycles with an average CE of 99.91% for Li||NMC811cells (Supplementary Fig. 49A). And, the CE can achieve 99.94% at a high rate of 1C (Supplementary Fig. 49B). This high stability at high voltage allows PTFEP-LPIFD to support Li||NMC811 cells at a high cut-off voltage to deliver a high capacity at a high C rate. As illustrated in Fig. 6F and Supplementary Fig. 50A, if the Li||NMC811 cell is limited to charging only up to 4.35V, a reversible specific capacity of 148.7 and 77 mAh g^{-1} can be delivered at a rate of 1C and 2C, respectively. The significantly lower capacity at 2C is attributed to overpotential and contact issues associated with polymer electrolytes. In comparison, the Li|PTFEP-LPIFD|NMC811 cell with a cut-off voltage of 4.6V delivers high reversible specific capacities of 186 and 101.2 mAh g^{-1} at 1C and 2C, respectively. At a higher working temperature of 45℃, by charging to 4.6V, the cell can even work at 2C, 3C, and 4C with high reversible capacities of 202.2, 146.7, and 105 mAh g^{-1} (Fig. 6F and Supplementary Fig. 50B, additional high-rate data is shown in Supplementary Fig. 51).

The high stability and high-rate capability observed in NMC811 can be attributed to the thin (<2nm) and uniform CEI in single-phase PTFEP-LPIFD (Fig. 6G). The cycled NMC811 particle surface maintains a layered structure without rock-salt structure, indicating the detrimental phase transition was effectively suppressed with PTFEP-LPIFD. This highly stable CEI remains

unchanged in thickness even after 200 cycles (Supplementary Fig. 52), which is also supported by the steady resistance evolution of Li|PTFEP-LPIFD|NMC811 full cells (Supplementary Fig. 53). XPS measurements were conducted to analyze the CEI composition. Compared to the cathode cycled in the commercial carbonate electrolytes (1M $LiPF_6$ in EC/DEC, Supplementary Fig. 54A-C), NMC811 cycled in PTFEP-LPIFD has a much stronger F signal owing to the high F content ratio in this LPIFD (Supplementary Fig. 54E). Moreover, significantly fewer O signals are observed (Supplementary Fig. 54D and 54F), indicating the excellent suppression capability in oxygen dissolution. Thermodynamically, these fluorine-containing species are much more resistant to oxidation than oxide species, which effectively suppress the side reaction on the cathode.

The Versatility of the LPIFD Concept

Our single-phase LPIFDs exhibit excellent mechanical properties as well as interfacial stability (i.e., by preventing dendrite growth and high voltage decomposition) at both electrodes. They can be fabricated easily. For these reasons, LPIFDs are attractive for application in various solid-state batteries (details in Supplementary Note 8). Ceramic electrolytes inherently possess grain boundaries that can facilitate the Li dendrite growth, while single-phase LPIFD can serve as an interlayer to prevent dendrite growth through grain boundaries, leading to an improved CE over 98 % and a high CCD of 3.7 mA cm^{-2} (Supplementary Fig. 55 and 56), allowing the Li||NMC811 full cell to achieve 150 cycles (Supplementary Fig. 57). Furthermore, an LPIFD can serve as the binder for polymer/ceramic hybrid composites, which allows for thin LPSC membranes that have improved stability with Li metal (Supplementary Fig. 58-61) and thereby enhance full cell performance (Supplementary Fig. 62). An LPIFD can also be used in a cell with micro-sized Si,

which can be cycled over 400 times (Supplementary Fig. 63). In this case, the LPIFD acts as a buffer against volume expansion and forms LiF-rich SEI to stabilize the Si anode.

Conclusions

We have designed single-phase, local-high-concentration polymer electrolytes by the high miscibility between Li-polymer and inert fluorinated diluter polymer. The single-phase LPIFD lacks phase boundaries, facilitating uniform Li deposition and ensuring a homogeneous LiF-rich SEI to stabilize the Li anode. Simultaneously, an F-rich CEI is formed to stabilize the NMC811 cathode at high voltage. As a result, the LPIFD achieves a high CE of 99.1% and a high CCD of 3.7 mA cm^{-2} on Li anodes, along with a high CE of 99.95% at 4.5V with a cycle life exceeding 450 cycles in Li||NMC811 cells. Moreover, Li||NMC811 cells can be charged to 4.6V with a high rate of up to 4C at 45^{o}C. The LPIFD concept can be extended to other solid-state electrolytes (e.g., ceramics) and in batteries with other electrodes (e.g., micro-sized Si anode). Thus, LPIFDs could prove to be the electrolytes of choice for a range of high-energy batteries.

Methods

Materials and Methods

Materials and Preparation of Electrolytes

Lithium bis(fluorosulfonyl)imide (LiFSI) was purchased from Nippon Shokubai. Poly(vinylidene fluoride-co-hexafluoropropylene) (PVDF-HFP, pellets), Poly(propylene carbonate) (PPC, average Mn ~50,000, pellets), Polyethylene oxide (PEO, average Mv 100,000, powder), Poly(methyl methacrylate) (PMMA, average Mw ~15,000, powder), and Poly(bis(2,2,2-trifluoroethoxy)phosphazene) (PTFEP, powder) were purchased from Sigma-Aldrich. All were dried at 90^{o}C under vacuum for 24 h to remove moisture. Ethenesulfonyl fluoride was used to synthesize the poly(vinylsulfonyl fluoride) (PVSF) by the reported method[81,82]. The basic information (Tg and Tm) of these polymers is listed in Supplementary Table 1. Acetonitrile (AN, $\geqslant$99.9%, boiling point 82 ^{o}C) and 1,2-Dimethoxyethane (DME, 99.9%, inhibitor-free, boiling point 85 ^{o}C) were bought from Sigma-Aldrich and dried overnight using molecular sieves.

All the fabrication processes, including the preparation of polymer electrolytes and the assembly of batteries, were done in an Ar-filled glovebox with H_2O content <0.1 ppm to avoid moisture in the air. The LPIFDs were made by the solution cast method. DME can dissolve most of the polymers in this work, thereby enhancing the accuracy of comparisons in different polymer electrolytes. In detail, all polymers (PMMA, PTFEP, PPC, PVSF, and PVDF-HFP) were dissolved separately in DME at a concentration of 5wt% (PVDF-HFP need to be dissolved by stirring on the hot plate at 55^{o}C), and in all cases, transparent polymer solutions were obtained. Because of the limited solubility of PEO in the DME, PEO alone was dissolved in the AN at 3wt%. Thereafter, the solution of PEO, PMMA, PTFEP, PPC, or PVSF (Li-polymer) was mixed with the solution of the PVDF-HFP (F-diluter) at a weight ratio of 1:2.5 to get polymer blends solution. Then the LiFSI

(63wt% in LPIFD) was added into the polymer blend solution to get the Li-polymer in the F-diluter (LPIFD) solution. The LPIFD solutions were then poured into Teflon dishes and dried at room temperature to evaporate most of the DME, then these membranes were further dried in a vacuum oven at 70^{o}C overnight and 75^{o}C for 2-3 hours to remove solvents. The LPIFD solid polymer electrolytes then were peeled off from dishes and cut into different sizes for testing.

The Li_6PS_5Cl (LPSC) solid electrolyte was prepared by milling Li_2S, P_2S_5, and LiCl at a stoichiometric ratio followed by annealing at 550 ^{o}C for 4h. LPSC pellets were made by pressing the LPSC electrolyte at 360 MPa. The PTFEP-LPIFD interlayer was formed by dropping 60-80µl of LPIFD solution on the surface of the LPSC pellet (20µl per time), followed by drying using the same conditions as above for forming LPIFD membranes.

LPSC membrane (Polytetrafluoroethylene, PTFE binder): The LPSC powder was hand milled with 1% PTFE and roll-pressed into a freestanding sheet. Then the sheet was pressed at 360 MPa to obtain thin solid electrolytes.

LPSC membrane (LPIFD binder): The LPSC powder was well dispersed into the PTFEP-LPIFD precursor solution, then the suspension was poured onto a Teflon dish and dried quickly at a high temperature of 70^{o}C and in vacuum. To get better mechanical properties, lower salt content (53wt% LiFSI) was used here. Then the sheet was pressed at 360 MPa to obtain thin solid electrolytes.

The composite cathode was created by directly filling a diluted polymer solution in the cathode and drying using the same process as above. Specifically, the LPIFD solution was diluted four times with DME, and then a certain amount of polymer solution was dropped on the $LiNi_{0.8}Mn_{0.1}Co_{0.1}O_2$ (NMC811) cathode and dried together with LPIFDs. Here, the un-calendered NMC811 cathode (95wt% active materials) coated on Al foil with a loading of around 1-1.3 mAh

cm^{-2} at 4.5V was kindly provided by Saft America, Inc. A loading of 2-3mg cm^{-2} cathode was used for the high-rate cycling test.

To coat the micro-silicon electrodes, a slurry was first prepared by dispersing silicon (Si) particles (APS 1-5 micron, 99.9% metals basis), lithium polyacrylate binder (10 wt% aqueous solutions) and C65 carbon black in water with a weight ratio of 6:2:2. The slurry was cast onto a copper (Cu) foil, dried at room temperature for 24 h and further dried at 90 °C overnight under vacuum. A composite Si-LPIFD anode was made by combining the Si anode with a diluted LPIFD solution in a manner identical to that used to make the composite cathode.

Electrochemical measurements.

Ionic conductivities of LPIFD membrane at different temperatures (25 ^{o}C – 80 ^{o}C) were determined by EIS over a frequency range of 1.0 MHz to 0.1 Hz on a gammary workstation using SS|LPIFD|SS coin cells (SS, stainless steel electrodes). Ionic conductivities were calculated by the equation 1:

$$\sigma = \frac{L}{R * S} \qquad \text{equation 1}$$

where L is thickness of the LPIFD, R presents the resistance value of the bulk electrolyte and S stands for the effective contacting area between the electrolyte and SS electrodes. Transference number t_+ was calculated by the following equation 2:

$$t_+ = \frac{I_s(\Delta V - I_0 R_0)}{I_0(\Delta V - I_S R_S)} \qquad \text{equation 2}$$

where ΔV is the voltage polarization applied, I_S and R_S are the steady state current and resistance, respectively, I_0 and R_0 are the initial current and resistance, respectively.

The cyclic voltammogram of the Li|LPIFD|Ti cells was tested with a scan rate of 1mV s^{-1} on a CHI 600E electrochemical workstation (CH Instruments USA). Interfacial stability of Li-electrolyte was conducted in the symmetric cell (Li|LPIFD|Li) with a Li with a diameter of 8mm. The CE of metallic Li was calculated using Li|LPIFD|Cu, rough copper is used to increase the contact between polymer electrolytes and Cu. The electrochemical performances of the Li metal batteries were all examined using 2032-type coin cells, which were assembled and disassembled in an Ar-filled glove box with O_2 and moisture content lower than 1 ppm. All the charge-discharge processes of Li||Cu, Li symmetrical, and Li||NCM811 full cells were tested using were investigated on LAND battery testing instrument at 30^{o}C or 35^{o}C when there is no specific comment. For galvanostatic tests of NMC811|LPIFD|Li cells, Ti was used to prevent the corrosion of LiFSI on the stainless steel when charging to the high voltage, a 14mm Ti was placed between the cathode and coin cell case, NCM 811 cathodes with diameter of 9mm or 9.5mm were coupled with 12mm polymer membrane so that the polymer membrane was not contacted with the coin cell case at the cathode side. As for the thin Li, a larger diameter of Li was used to avoid the contact of the cathode and anode. The cells were charged/discharged between a voltage range of 2.8 V-4.35 V, 2.8V-4.5V, and 2.8V-4.6V and two formation cycles at C/10 were first conducted before long-term cycling at a higher current density of C/2. Cyclic voltammetry (CV), and electrochemical impedance spectroscopy (EIS) were all conducted on a CHI 600E electrochemical workstation (CH Instruments Inc. USA). Two-electrode Li|LPSC|Li symmetric cell was assembled in solid state cell mold by attaching Li foil on both sides of the electrolyte pellet, the stack pressure was about 2.0 MPa. For LPSC with PTFEP-LPIFD interlayer, both Li||Li cell and composite NMC811||Li cells were tested in coin cells due to the good contact of electrolyte with lithium.

Characterizations.

FTIR was recorded by the NEXUS 670 FTIR instrument. The morphologies were characterized using an SEM. The SEM and high-resolution TEM images in the present work were taken at the University of Maryland using Hitachi SU-70 analytical GEG SEM (Japan) and JEOL JEM (Japan) 2100 LaB6 transmission electron microscope with an electron accelerating voltage of 200 KeV, respectively. All the electrodes after cycling were rinsed in DME (DME/AN for PEO-LPIFD) several times to remove any residual polymer electrolytes, X-ray photoelectron spectroscopy (XPS) measurements were acquired with a K-alpha Thermo system using Al Kα radiation (hν = 1486.6 eV) under ultra-high vacuum (<1x10-12 atm) with a measured spot size of 400 μm in diameter. A flood gun was used during the analysis to compensate for the charging of the samples. The samples were transferred from the argon glove box into the XPS chamber with a vacuum transfer vessel to avoid exposure to air. Sputter depth profiling was carried out using an Ar+ ion gun with ion energy at 200 eV with a roster size of 2 mm. The angle between the surface normal and the ion gun beam was 0°. A sputter procedure of two times for 60 s, one time for 180 s, and one time for 300 s was used. The binding energy was corrected based on the C1s spectrum, assigning C-C to 285 eV. Relative atomic concentrations were calculated by integrating respective peaks with a Shirley background, using The CasaXPS software, accounting for respective atomic sensitivity factors.

STXM measurements were performed at the SM beamline of the Canadian Light Source (CLS). The polymer electrolyte was spin-coated on Si3N4 windows for STXM study at C, O, and F K-edges. In STXM, the monochromatic X-ray beam is focused by a Fresnel zone plate to a 30 nm spot on the sample, and the sample is raster-scanned with synchronized detection of transmitted X-rays to generate image sequences (stacks) over a range of photon energies. The obtained STXM data were analyzed using aXis2000 (http://unicorn.mcmaster.ca/aXis2000.html). The principle component analysis (PCA) and the following cluster analysis (CA) of the STXM data were performed using the PCA_GUI 1.1.1 (Stony Brook University) free software[83].

Soft X-ray Absorption Spectroscopy (sXAS). The oxygen K-edge XAS spectra were measured in total electron yield (TEY) at 23-ID-2 beamline (IOS) of National Synchrotron Light Source II (NSLS II), Brookhaven National Laboratory (BNL). The data was analyzed using the Athena software[84].

All rheological experiments were done on an HR 20 Discovery Hybrid Rheometer (TA Instruments) at 60 °C or 100°C using a parallel plate geometry (25 mm diameter). For the oscillatory shear (dynamic rheology) experiments, polymer or solid polymer electrolyte samples were cut into discs of 20 mm diameter. Through stress-sweep experiments, the linear viscoelastic region of the samples was obtained, and a strain (0.5%) within this region was used to run the frequency-sweep experiments.

Quantification solution ^{1}H NMR experiments for all samples were run at a Bruker AVANCE III 600 MHz NMR spectrometer with a BBFO probe. The polymer electrolytes were dissolved in the DMSO at 50^{o}C with stirring for one night. One pulse program with a pulse delay of 30 s and 16 scans was employed to collect ^{1}H NMR spectra with reference to TMS. Solid-state ^{7}Li NMR spectra with magic angle spinning (MAS) of all samples were collected on a Bruker Avance NEO solid-state 500 MHz NMR spectrometer with a double resonance H/F-X probe. Briefly, samples were packed in a 3.2-mm outer diameter zirconia rotor with Kel-F endcap spinning at 10 and 8 kHz. One pulse program was used with the $\pi/2$ pulse length of 2.5 μs and a recycle delay of 5 s. Each ^{7}Li NMR spectrum was collected with 128 scans and the line broadening for the spectrum was 20 Hz. The ^{7}Li NMR spectrum was referenced to 10M LiCl in the D2O solution by setting the ^{7}Li chemical shift at 0 ppm.

Computational details

Molecular dynamics simulation. For classical molecular dynamics simulation (MD), the LPIFD systems composing three different polymer blends based on PVDF-HFP and conductive PEO, PMMA and PTFEP, and LiFSI salt were assembled so that to keep the same composition used in the experiment, namely 1:0.4:2.4. The non-polarizable all-atomic OPLS(-AA), "Optimized Potentials for Liquid Simulations", force field[85,86] as available in Gromacs simulation package[87–91] database, was utilized to adjust most of the intra- and intermolecular potential parameters, describing covalent terms within bond stretching, angle bending and dihedral angle torsion along the covalent bond, and non-covalent terms represented by the van der Waals and Coulomb interactions. In the case of PTFEP, all the missing intermolecular parameters related to −P=N− bond were generated using a modified version of OPLS-AA(-M) [92] of LigParGen web service[93]. The Coulomb interactions were described by the partial charges evaluated in the framework Merz-Singh-Kollman scheme[94] based on trimmer configuration. The latter was initially optimized using HF/6-31G(d) level of theory, followed by the analysis in MP2/cc-pVTZ as available in Gaussian 16[95].

For each of the polymer, a chain length of 50 monomers was selected. To keep the amorphous structure of PVDF-HFP the VDF: HFP molar ratio has been set to 4:1[96–99], while maintaining the VDF/HFP monomer sequence reported previously[96,99]. Each initial system containing ~50000 atoms was generated by Packmol and placed into an orthorhombic box of 20×20×60 nm with three-dimensional periodic boundary conditions. Such system size was selected to avoid deleterious pressure fluctuations and to reduce the influence of the on finite size effects on the polymer dynamics and electrostatic interactions during the equilibration stage[100], while a considerable larger box was taken to avoid the intermolecular/interchain clashes.

All MD simulations were carried out using Gromacs, version 2016.3. Equations of motion were integrated using leap-frog algorithm[101] with a time-step of 2×10^{-6} ns. The time-step selection was

justified by utilization of C−H bonds constraints, which was achieved with LINCS, "LINear Constraint Solver", algorithm[102]. The electrostatic long-range interactions within the cut-off range of 1.4 nm were accounted by the computationally efficient Particle Mesh Ewald algorithm[103], using the same cut-off distance for the real-space component. The 12-6 Lennard-Jones interactions were treated by the conventional shifted force technique with a switch region between 1.2 and 1.3 nm. Cross interactions between different atom types were derived using standard Lorentz-Berthelot combination rule.

The considered LPIFD systems were energy-minimized using steepest descent algorithm followed by the series of equilibration steps in an isothermal-isobaric (*n*pT) and canonical (*n*VT) ensembles, where to facilitate blending process and to reduce computational costs at certain steps temperature was increased by 230 or 330 K with respect to experimental conditions: (1) 0.1 ns of *n*pT compression at 1 kbar and 533 K; (2) 0.1 ns of *n*pT compression at 4 kbar and 533 K; (3) 0.5 ns of *n*pT compression at 4 kbar and 533 K; (4) 1 ns of *n*pT relaxation at 0.001 kbar and 533 K; (5) 0.5 ns of *n*pT heating at 0.001 kbar and 633 K; (6) 0.5 ns of *n*pT cooling at 0.001 kbar and 533 K; (7) 1 ns of *n*VT relaxation at 533 K; (8) 6.3 ns *n*pT relaxation at 0.001 kbar and 533 K; (9) 1000 ns *n*pT blending at 0.001 kbar and 533 K; (10) 200 ns *n*pT cooling 0.001 kbar and 303 K according to experimental conditions. For steps 1-8, the temperature and pressure were kept constant by applying Berendsen thermostat and barostat[104] with coupling constants of 3×10^{-4} and 5×10^{-4} ns, respectively, while for step 8 a velocity-rescaling[105] thermostat and Parrinello-Rahman barostat[106] was set with further substitution by Nose-Hoover thermostat (8×10^{-4} ns) for the last steps 9-10. All the structure properties presented in this work were derived from an additional 10 ns *n*VT trajectory by saving coordinates each 1×10^{-3} ns and additionally enhanced by Travis code [107,108] version May 21, 2021.

Geometry optimization. Initial geometry configurations obtained from the molecular dynamic simulations were cut down to limit the polymeric repeating units to only two-to-three units of PMMA, PEO, and PFTEP, and are in close proximity to (interacting with) the LiFSI. The cutdown was made to limit the computational costs in performing quantum chemistry calculations. The generated structures were then optimized using the GFN2-XTB method[109] – an accurate and broadly parametrized self-consistent tight-binding method. The optimized geometries were used in calculating X-Ray Absorption Spectra (XAS).

X-Ray absorption spectra (XAS) theoretical calculations. All calculations were performed using the ORCA software of version 5.0.3[110]. The Oxygen K-edge XAS spectra were calculated using density functional theory (DFT) combined with Restricted Open Shell Configuration Interaction with Singles (DFT-ROCIS) method[111]. This method was chosen as it was reported in several studies as an excellent method in predicting experimental XAS measurements accurately[112]. Throughout our calculations, B3LYP[113,114] functional was used with the Ahlrichs polarized def2-TZVP basis sets[115,116] together with the auxiliary def2/J[117,118] to accelerate the calculations in presence of RIJCOSX approximations. Additionally, scalar relativistic effects were implemented by employing ZORA[119] corrections explicitly. Scaling parameters of c1=0.18, c2=0.20 and c3=0.40 were used as they were proven to be the best set of parameters for a chosen test set[111]. The excitation window was constructed specifying one donor space corresponding to the excitation donor orbitals and an acceptor orbital space that corresponds to all singly occupied states and the entire virtual orbitals space. A total of 100 roots were requested to cover as many single excitation states as possible. The data files for generating plots were produced using a utility called Orca_mapspc that was integrated in the Orca program suite. The peaks were normalized and a constant energy shift of +13.2 to +15 eV was made to match with the pre-edge peaks energy positions of the experimental measurements.

Data and materials availability: All data are available in the main text or the supplementary materials.

Acknowledgments: We acknowledge the advice on the manuscript from Dr. Bruce Dunn at the University of California, Los Angeles, and technical support from the Maryland NanoCenter. STXM was performed at the Canadian Light Source, a national research facility of the University of Saskatchewan. We thank the computational resources provided on Bebop, a high-performance computing cluster operated by the Laboratory Computing Resource Center at Argonne National Laboratory. This work was supported by the Department of Energy (DOE) grant DE-EE0008856 (C. W.), and the Department of Energy (DOE), Office of Energy Efficiency and Renewable Energy (EERE) grant DE-EE0009183 (C. W.). The XAS test was supported by Department of Energy (DOE), Battery500 Consortium grant DE-SC0012704 (S. T, X. Y. & E. H.), and Department of Energy (DOE), Office of Science User Facilities DE-SC0012704 (BNL). We also thank the Analytical NMR Service & Research Center at the University of Maryland, College Park for using 600 MHz solution and 500 MHz solid-state (supported by NSF: NSF-1726058) NMR spectrometers.

Author contributions: W.Z. and C.W. proposed the research. W.Z. conceived the idea; performed electrochemical, SEM, and TEM experiments; and wrote the manuscript. V.K. and N.D. performed molecular dynamics simulations and DFT calculations. S.L. helped with electrochemical experiments and the SEM. P.B. helped on FTIR. J.Z. and J.W. performed the STXM, S.T., X.Y., and E.H. performed the XAS. Z.W. helped with the analysis of calculation results. J.X., H.W, and X.Z. helped with the manuscript editing. H.Y performed the Instron mechanical test. B.N., B.L., and A.L. performed XPS and analysis of results. F.C. performed the NMR. S.R. drew the schematic edited the manuscript and supervised the analysis of the polymer properties. A.N. supervised the simulations and calculations, and C.W. supervised the study and the manuscript writing. All authors discussed the results.

Competing interests: Authors declare that they have no competing interests.

Figure Legends/Captions:

Fig. 1. The schematic of the logic to design single-phase Li-polymer in F-diluter (LPIFD) solid polymer electrolytes. (**A**) Salt in polymer electrolytes. (**B**) Polymer in salt electrolytes. (**C**) Phase-separated LPIFD. (**D**) Single-phase LPIFD.

Fig. 2. Li-polymer in F-diluter (LPIFD) solid polymer electrolyte design. LPIFD electrolytes are composed of F-diluter: PVDF-HFP; and Li-polymer: LiFSI with 1. PPC, 2. PEO, 3. PMMA, 4. PVSF, 5. PTFEP.

Fig. 3. Properties of phase-separated and single-phase LPIFD (**A-F**) STXM images and C K-edges of (A and D) PEO-LPIFD, (B and E) PMMA-LPIFD and (C and F) PTFEP-LPIFD. (**G-I**) Snapshots of equilibrated structures and density profiles of (G) phase-separated PEO-LPIFD, (H) single-phase PMMA-LPIFD, and (I) PTFEP-LPIFD simulated by molecular dynamics. The direction of the normal vector of the X-axis of the equilibrated cell represents the concentration distribution of the constituents. Yellow beads stand for FSI, red part for PEO/PMMA/PTFEP, and green part for PVDF-HFP. (**J**) Oxygen K-edge XAS spectra of PEO/PVDF-HFP polyblends and PEO-LPIFD, PMMA/PVDF-HFP polyblends and PMMA-LPIFD, PTFEP/PVDF-HFP polyblends and PTFEP-LPIFD. (**K**) FTIR spectra of PTFEP, PVDF-HFP, PTFEP/PVDF-HFP blends, and PTFEP-LPIFD polymer electrolytes.

Fig. 4. SEI composition and electrochemical performance of LPIFD polymer electrolytes with lithium. Quantified atomic composition ratios of the SEI at different sputtering times (0s, 120s, 300s, 600s, 1200s from top to bottom) for (**A**) PEO-LPIFD, (**B**) PMMA-LPIFD, and (**C**) PTFEP-LPIFD. (**D**) The cycling profile for Li symmetric cells of Li|PEO-LPIFD|Li, Li|PMMA-LPIFD|Li, and Li|PTFEP-LPIFD|Li at a current density of 0.5 mA cm^{-2} with 1h/1h plating/stripping time. (**E**) Coulombic efficiency of PEO-LPIFD (0.3 mA cm^{-2}), PMMA-LPIFD (0.3 mA cm^{-2}), PTFEP-LPIFD (0.5 mA cm^{-2}). (**F**) Li-metal plating/stripping profiles of Li|PTFEP-LPIFD|Cu cell.

Fig. 5. **The different Li deposition behavior of LPIFDs, and summary of design criteria.** The morphology of metallic Li deposited on the Cu substrate with (**A-C**) PEO-LPIFD (0.3 mA cm^{-2}, 0.6 mAh cm^{-2}), (**D-F**) PMMA-LPIFD (0.3 mA cm^{-2}, 1 mAh cm^{-2}), (**G-I**) PTFEP-LPIFD (0.5 mA cm^{-2}, 2 mAh cm^{-2}). To ensure consistency, the current density used for deposition is the same as

that of the CE test. (**J**) Table of summary for Li||Cu CEs and CCDs of different LPIFDs with different Li-polymers.

Fig. 6. Full cell performance of single-phase LPIFD. (**A**) Electrochemical stability window of PTFEP-LPIFD. (**B**) Voltage profiles, (**C**) cycling performance, and (**D**) average discharge voltage of the coin cells with NMC811 cathodes at 4.5V cut-off voltage using PTFEP-LPIFD. Cycling performance of (**E**) homemade pouch cell (N/P 4.3) with 20μm Li foil with at 4.35V cut-off voltage using PTFEP-LPIFD, the dimension of the electrode in pouch cell is 3.7cm x 3.7cm, the C-rate is 0.3C. (**F**) Rate performance (1C = 200 mAh g^{-1}, with capacity retention at right Y axis) at 30℃ and 45℃ at 4.35V vs 4.6 V cut-off voltage using PTFEP-LPIFD. During the rate test, both of them are charged to 4.6V in the first cycle to ensure that the same CEI is formed. (**G**) TEM images of cycled NMC811 electrodes collected from Li|PTFEP-LPIFD|NMC811 cell after 100 cycles.

References

1. Lin, D., Liu, Y. & Cui, Y. Reviving the lithium metal anode for high-energy batteries. *Nat Nanotechnol* **12**, 194–206 (2017).
2. Lu, Y., Tu, Z. & Archer, L. A. Stable lithium electrodeposition in liquid and nanoporous solid electrolytes. *Nat Mater* **13**, 961–969 (2014).
3. Huang, W., Feng, X., Han, X., Zhang, W. & Jiang, F. Questions and answers relating to lithium-ion battery safety issues. *Cell Rep Phys Sci* **2**, 100285 (2021).
4. Bai, P., Li, J., Brushett, F. R. & Bazant, M. Z. Transition of lithium growth mechanisms in liquid electrolytes. *Energy Environ Sci* **9**, 3221–3229 (2016).
5. Li, W. *et al.* The synergetic effect of lithium polysulfide and lithium nitrate to prevent lithium dendrite growth. *Nat Commun* **6**, 1–8 (2015).
6. Ren, Y., Shen, Y., Lin, Y. & Nan, C.-W. Direct observation of lithium dendrites inside garnet-type lithium-ion solid electrolyte. *Electrochem commun* **57**, 27–30 (2015).
7. Xu, K. Nonaqueous liquid electrolytes for lithium-based rechargeable batteries. *Chem Rev* **104**, 4303–4418 (2004).
8. Cheng, X.-B., Zhang, R., Zhao, C.-Z. & Zhang, Q. Toward safe lithium metal anode in rechargeable batteries: a review. *Chem Rev* **117**, 10403–10473 (2017).
9. Liu, S. *et al.* In situ solid electrolyte interphase from spray quenching on molten Li: a new way to construct high-performance lithium-metal anodes. *Advanced Materials* **31**, 1806470 (2019).
10. Paul, P. P. *et al.* A Review of Existing and Emerging Methods for Lithium Detection and Characterization in Li-Ion and Li-Metal Batteries. *Adv Energy Mater* **11**, 2100372 (2021).
11. Park, R. J.-Y. *et al.* Semi-solid alkali metal electrodes enabling high critical current densities in solid electrolyte batteries. *Nat Energy* **6**, 314–322 (2021).
12. Fan, X. *et al.* Fluorinated solid electrolyte interphase enables highly reversible solid-state Li metal battery. *Sci Adv* **4**, eaau9245 (2018).
13. Ji, X. *et al.* Solid-State Electrolyte Design for Lithium Dendrite Suppression. *Advanced Materials* **32**, 2002741 (2020).
14. Ren, Y. X. *et al.* Rational design of spontaneous reactions for protecting porous lithium electrodes in lithium–sulfur batteries. *Nat Commun* **10**, 1–10 (2019).
15. Fan, X. *et al.* Non-flammable electrolyte enables Li-metal batteries with aggressive cathode chemistries. *Nat Nanotechnol* **13**, 715–722 (2018).
16. Wang, J. *et al.* Superconcentrated electrolytes for a high-voltage lithium-ion battery. *Nat Commun* **7**, 1–9 (2016).
17. Yamada, Y. & Yamada, A. Superconcentrated electrolytes for lithium batteries. *J Electrochem Soc* **162**, A2406 (2015).
18. Chen, J. *et al.* Electrolyte design for LiF-rich solid–electrolyte interfaces to enable high-performance microsized alloy anodes for batteries. *Nat Energy* **5**, 386–397 (2020).
19. Fan, X. *et al.* Highly fluorinated interphases enable high-voltage Li-metal batteries. *Chem* **4**, 174–185 (2018).
20. Cao, X. *et al.* Monolithic solid–electrolyte interphases formed in fluorinated orthoformate-based electrolytes minimize Li depletion and pulverization. *Nat Energy* **4**, 796–805 (2019).
21. Ren, X. *et al.* Localized high-concentration sulfone electrolytes for high-efficiency lithium-metal batteries. *Chem* **4**, 1877–1892 (2018).

22. Yu, Z. *et al.* Molecular design for electrolyte solvents enabling energy-dense and long-cycling lithium metal batteries. *Nat Energy* **5**, 526–533 (2020).
23. Monroe, C. & Newman, J. The impact of elastic deformation on deposition kinetics at lithium/polymer interfaces. *J Electrochem Soc* **152**, A396 (2005).
24. Monroe, C. & Newman, J. The effect of interfacial deformation on electrodeposition kinetics. *J Electrochem Soc* **151**, A880 (2004).
25. Krauskopf, T., Richter, F. H., Zeier, W. G. & Janek, J. Physicochemical concepts of the lithium metal anode in solid-state batteries. *Chem Rev* **120**, 7745–7794 (2020).
26. Cao, D. *et al.* Lithium dendrite in all-solid-state batteries: growth mechanisms, suppression strategies, and characterizations. *Matter* **3**, 57–94 (2020).
27. Lu, Y. *et al.* Critical current density in solid-state lithium metal batteries: Mechanism, influences, and strategies. *Adv Funct Mater* **31**, 2009925 (2021).
28. Wang, Y. *et al.* Solid-state rigid-rod polymer composite electrolytes with nanocrystalline lithium ion pathways. *Nat Mater* **20**, 1255–1263 (2021).
29. Zhao, Q., Liu, X., Stalin, S., Khan, K. & Archer, L. A. Solid-state polymer electrolytes with in-built fast interfacial transport for secondary lithium batteries. *Nat Energy* **4**, 365–373 (2019).
30. Cabañero Martínez, M. A. *et al.* Are Polymer-Based Electrolytes Ready for High-Voltage Lithium Battery Applications? An Overview of Degradation Mechanisms and Battery Performance. *Adv Energy Mater* **12**, 2201264 (2022).
31. Lin, R. *et al.* Characterization of the structure and chemistry of the solid–electrolyte interface by cryo-EM leads to high-performance solid-state Li-metal batteries. *Nat Nanotechnol* **17**, 768–776 (2022).
32. Holoubek, J. *et al.* Tailoring electrolyte solvation for Li metal batteries cycled at ultra-low temperature. *Nat Energy* **6**, 303–313 (2021).
33. Gao, H., Grundish, N. S., Zhao, Y., Zhou, A. & Goodenough, J. B. Formation of stable interphase of polymer-in-salt electrolyte in all-solid-state lithium batteries. *Energy Material Advances* **2021**, (2021).
34. Chen, F., Wang, X., Armand, M. & Forsyth, M. Cationic polymer-in-salt electrolytes for fast metal ion conduction and solid-state battery applications. *Nat Mater* 1–8 (2022).
35. Kimura, K., Yajima, M. & Tominaga, Y. A highly-concentrated poly (ethylene carbonate)-based electrolyte for all-solid-state Li battery working at room temperature. *Electrochem commun* **66**, 46–48 (2016).
36. Fan, R. *et al.* Versatile strategy for realizing flexible room-temperature all-solid-state battery through a synergistic combination of salt affluent PEO and Li6. 75La3Zr1. 75Ta0. 25O12 nanofibers. *ACS Appl Mater Interfaces* **12**, 7222–7231 (2020).
37. Wang, X. *et al.* Lithium-salt-rich PEO/Li0. 3La0. 557TiO3 interpenetrating composite electrolyte with three-dimensional ceramic nano-backbone for all-solid-state lithium-ion batteries. *ACS Appl Mater Interfaces* **10**, 24791–24798 (2018).
38. Wu, J. *et al.* Reducing the thickness of solid-state electrolyte membranes for high-energy lithium batteries. *Energy Environ Sci* **14**, 12–36 (2021).
39. Wang, X. *et al.* Ultra-stable all-solid-state sodium metal batteries enabled by perfluoropolyether-based electrolytes. *Nat Mater* 1–9 (2022).
40. Zhao, Y. *et al.* A rational design of solid polymer electrolyte with high salt concentration for lithium battery. *J Power Sources* **407**, 23–30 (2018).
41. Cheng, X.-B., Zhao, C.-Z., Yao, Y.-X., Liu, H. & Zhang, Q. Recent advances in energy chemistry between solid-state electrolyte and safe lithium-metal anodes. *Chem* **5**, 74–96 (2019).

42. Han, F. *et al.* High electronic conductivity as the origin of lithium dendrite formation within solid electrolytes. *Nat Energy* **4**, 187–196 (2019).
43. Wu, B. *et al.* The role of the solid electrolyte interphase layer in preventing Li dendrite growth in solid-state batteries. *Energy Environ Sci* **11**, 1803–1810 (2018).
44. Wu, Q. *et al.* Phase regulation to obtain dense composite polymer-based electrolytes for high-voltage solid-state lithium metal batteries. (2023).
45. Xi, J. *et al.* PVDF–PEO blends based microporous polymer electrolyte: effect of PEO on pore configurations and ionic conductivity. *J Power Sources* **157**, 501–506 (2006).
46. Chaput, S., Carrot, C., Castro, M. & Prochazka, F. Co-continuity interval in immiscible polymer blends by dynamic mechanical spectroscopy in the molten and solid state. *Rheol Acta* **43**, 417–426 (2004).
47. Liu, J. *et al.* Blending-based poly (vinylidene fluoride)/polymethyl methacrylate membrane for rechargeable lithium-ion batteries. *Ionics (Kiel)* **25**, 5201–5211 (2019).
48. Cznotka, E., Jeschke, S., Schmohl, S., Johansson, P. & Wiemhöfer, H.-D. 3D laser scanning confocal microscopy of siloxane-based comb and double-comb polymers in PVDF-HFP thin films. *J Coat Technol Res* **13**, 577–587 (2016).
49. Tang, L. *et al.* Polyfluorinated crosslinker-based solid polymer electrolytes for long-cycling 4.5 V lithium metal batteries. *Nat Commun* **14**, 2301 (2023).
50. Zhang, X. *et al.* Self-suppression of lithium dendrite in all-solid-state lithium metal batteries with poly (vinylidene difluoride)-based solid electrolytes. *Advanced materials* **31**, 1806082 (2019).
51. Liu, W. *et al.* Designing polymer-in-salt electrolyte and fully infiltrated 3D electrode for integrated solid-state lithium batteries. *Angewandte Chemie* **133**, 13041–13050 (2021).
52. Zhang, W., Yi, Q., Li, S. & Sun, C. An ion-conductive Li7La3Zr2O12-based composite membrane for dendrite-free lithium metal batteries. *J Power Sources* **450**, 227710 (2020).
53. Guo, S. *et al.* PVDF-HFP/LiF composite interfacial film to enhance the stability of Li-metal anodes. *ACS Appl Energy Mater* **3**, 7191–7199 (2020).
54. Borodin, O. Challenges with prediction of battery electrolyte electrochemical stability window and guiding the electrode–electrolyte stabilization. *Curr Opin Electrochem* **13**, 86–93 (2019).
55. Yang, Z., Zhang, W., Li, J. & Chen, J. Polyphosphazene membrane for desulfurization: Selecting poly [bis (trifluoroethoxy) phosphazene] for pervaporative removal of thiophene. *Sep Purif Technol* **93**, 15–24 (2012).
56. Kaskhedikar, N. *et al.* Ionic conductivity of polymer electrolyte membranes based on polyphosphazene with oligo (propylene oxide) side chains. *Solid State Ion* **177**, 703–707 (2006).
57. Jankowsky, S., Hiller, M. M. & Wiemhöfer, H.-D. Preparation and electrochemical performance of polyphosphazene based salt-in-polymer electrolyte membranes for lithium ion batteries. *J Power Sources* **253**, 256–262 (2014).
58. Yu, Z. *et al.* Rational solvent molecule tuning for high-performance lithium metal battery electrolytes. *Nat Energy* **7**, 94–106 (2022).
59. Xu, S. *et al.* Decoupling of ion pairing and ion conduction in ultrahigh-concentration electrolytes enables wide-temperature solid-state batteries. *Energy Environ Sci* **15**, 3379–3387 (2022).
60. Wang, J., Zhou, J., Hu, Y. & Regier, T. Chemical interaction and imaging of single Co 3 O 4/graphene sheets studied by scanning transmission X-ray microscopy and X-ray absorption spectroscopy. *Energy Environ Sci* **6**, 926–934 (2013).

61. Schmeißer, D. *et al.* Characterization of oxidic and organic materials with synchrotron radiation based XPS and XAS. *Materials Science (0137-1339)* **27**, (2009).
62. Widstrom, M. D. *et al.* Water domain enabled transport in polymer electrolytes for lithium-ion batteries. *Macromolecules* **54**, 2882–2891 (2021).
63. Chen, L. *et al.* A 63 m superconcentrated aqueous electrolyte for high-energy Li-ion batteries. *ACS Energy Lett* **5**, 968–974 (2020).
64. Piao, N. *et al.* Countersolvent electrolytes for lithium-metal batteries. *Adv Energy Mater* **10**, 1903568 (2020).
65. Smith, J. W. *et al.* X-Ray absorption spectroscopy of LiBF 4 in propylene carbonate: a model lithium ion battery electrolyte. *Physical Chemistry Chemical Physics* **16**, 23568–23575 (2014).
66. Ong, M. T. *et al.* Lithium ion solvation and diffusion in bulk organic electrolytes from first-principles and classical reactive molecular dynamics. *J Phys Chem B* **119**, 1535–1545 (2015).
67. Wu, C. H. *et al.* Molecular-scale structure of electrode–electrolyte interfaces: the case of platinum in aqueous sulfuric acid. *J Am Chem Soc* **140**, 16237–16244 (2018).
68. Yamane, H. *et al.* Critical absorbed dose of resinous adhesive material towards non-destructive chemical-state analysis using soft x-rays. *J Electron Spectros Relat Phenomena* **232**, 11–15 (2019).
69. Zhou, D. *et al.* In situ synthesis of a hierarchical all-solid-state electrolyte based on nitrile materials for high-performance lithium-ion batteries. *Adv Energy Mater* **5**, 1500353 (2015).
70. Deng, T. *et al.* In situ formation of polymer-inorganic solid-electrolyte interphase for stable polymeric solid-state lithium-metal batteries. *Chem* **7**, 3052–3068 (2021).
71. Wu, N. *et al.* In situ formation of Li3P layer enables fast Li+ conduction across Li/solid polymer electrolyte interface. *Adv Funct Mater* **30**, 2000831 (2020).
72. Fan, X. *et al.* All-temperature batteries enabled by fluorinated electrolytes with non-polar solvents. *Nat Energy* **4**, 882–890 (2019).
73. Chen, J. *et al.* Electrolyte design for Li metal-free Li batteries. *Materials Today* **39**, 118–126 (2020).
74. Bhattacharyya, R. *et al.* In situ NMR observation of the formation of metallic lithium microstructures in lithium batteries. *Nat Mater* **9**, 504–510 (2010).
75. Chandrashekar, S. *et al.* 7Li MRI of Li batteries reveals location of microstructural lithium. *Nat Mater* **11**, 311–315 (2012).
76. Tsai, C.-L. *et al.* Li7La3Zr2O12 interface modification for Li dendrite prevention. *ACS Appl Mater Interfaces* **8**, 10617–10626 (2016).
77. Liu, S. *et al.* An inorganic-rich solid electrolyte interphase for advanced lithium-metal batteries in carbonate electrolytes. *Angewandte Chemie International Edition* **60**, 3661–3671 (2021).
78. Liu, S. *et al.* Salt-in-Salt Reinforced Carbonate Electrolyte for Li Metal Batteries. *Angewandte Chemie International Edition* (2022).
79. Cabañero Martínez, M. A. *et al.* Are Polymer-Based Electrolytes Ready for High-Voltage Lithium Battery Applications? An Overview of Degradation Mechanisms and Battery Performance. *Adv Energy Mater* **12**, 2201264 (2022).
80. Xu, K. Electrolytes and interphases in Li-ion batteries and beyond. *Chem Rev* **114**, 11503–11618 (2014).

81. Fujigaya, T. *et al.* New photoresist materials for 157-nm lithography. poly [vinylsulfonyl fluoride-co-4-(1, 1, 1, 3, 3, 3-hexafluoro-2-hydroxypropyl)-styrene] partially protected with tert-butoxycarbonyl. *Chemistry of materials* **15**, 1512–1517 (2003).
82. Gao, Y. *et al.* Polymer–inorganic solid–electrolyte interphase for stable lithium metal batteries under lean electrolyte conditions. *Nat Mater* **18**, 384–389 (2019).
83. Lerotic, M., Jacobsen, C., Schäfer, T. & Vogt, S. Cluster analysis of soft X-ray spectromicroscopy data. *Ultramicroscopy* **100**, 35–57 (2004).
84. Ravel, B. & Newville, M. ATHENA, ARTEMIS, HEPHAESTUS: data analysis for X-ray absorption spectroscopy using IFEFFIT. *J Synchrotron Radiat* **12**, 537–541 (2005).
85. Jorgensen, W. L. & Tirado-Rives, J. The OPLS [optimized potentials for liquid simulations] potential functions for proteins, energy minimizations for crystals of cyclic peptides and crambin. *J Am Chem Soc* **110**, 1657–1666 (1988).
86. Jorgensen, W. L., Maxwell, D. S. & Tirado-Rives, J. Development and testing of the OPLS all-atom force field on conformational energetics and properties of organic liquids. *J Am Chem Soc* **118**, 11225–11236 (1996).
87. Abraham, M. J. *et al.* GROMACS: High performance molecular simulations through multi-level parallelism from laptops to supercomputers. *SoftwareX* **1**, 19–25 (2015).
88. Pronk, S. *et al.* GROMACS 4.5: a high-throughput and highly parallel open source molecular simulation toolkit. *Bioinformatics* **29**, 845–854 (2013).
89. Hess, B., Kutzner, C., van der Spoel, D. & Lindahl, E. GROMACS 4: algorithms for highly efficient, load-balanced, and scalable molecular simulation. *J Chem Theory Comput* **4**, 435–447 (2008).
90. van der Spoel, D. *et al.* GROMACS: fast, flexible, and free. *J Comput Chem* **26**, 1701–1718 (2005).
91. Berendsen, H. J. C., van der Spoel, D. & van Drunen, R. GROMACS: A message-passing parallel molecular dynamics implementation. *Comput Phys Commun* **91**, 43–56 (1995).
92. Robertson, M. J., Tirado-Rives, J. & Jorgensen, W. L. Improved peptide and protein torsional energetics with the OPLS-AA force field. *J Chem Theory Comput* **11**, 3499–3509 (2015).
93. Dodda, L. S., Cabeza de Vaca, I., Tirado-Rives, J. & Jorgensen, W. L. LigParGen web server: an automatic OPLS-AA parameter generator for organic ligands. *Nucleic Acids Res* **45**, W331–W336 (2017).
94. Singh, U. C. & Kollman, P. A. An approach to computing electrostatic charges for molecules. *J Comput Chem* **5**, 129–145 (1984).
95. Frisch, M. J. *et al.* Gaussian 16 Rev. C. 01, Wallingford, CT. Preprint at (2016).
96. Twum, E. B., McCord, E. F., Lyons, D. F., Fox, P. A. & Rinaldi, P. L. Characterization of end groups and branching structures in copolymers of vinylidene fluoride with hexafluoropropylene using multidimensional NMR spectroscopy. *Eur Polym J* **51**, 136–150 (2014).
97. Apostolo, M., Arcella, V., Storti, G. & Morbidelli, M. Kinetics of the emulsion polymerization of vinylidene fluoride and hexafluoropropylene. *Macromolecules* **32**, 989–1003 (1999).
98. Ameduri, B., Boutevin, B. & Kostov, G. Fluoroelastomers: synthesis, properties and applications. *Prog Polym Sci* **26**, 105–187 (2001).
99. Twum, E. B., McCord, E. F., Fox, P. A., Lyons, D. F. & Rinaldi, P. L. Characterization of backbone structures in poly (vinylidene fluoride-co-hexafluoropropylene) copolymers by multidimensional 19F NMR spectroscopy. *Macromolecules* **46**, 4892–4908 (2013).

100. Gartner III, T. E. & Jayaraman, A. Modeling and simulations of polymers: a roadmap. *Macromolecules* **52**, 755–786 (2019).
101. Hockney, R. W., Goel, S. P. & Eastwood, J. W. Quiet high-resolution computer models of a plasma. *J Comput Phys* **14**, 148–158 (1974).
102. Hess, B., Bekker, H., Berendsen, H. J. C. & LINCS, J. F. A linear constraint solver for molecular simulations. *J Comput Chem* (1977).
103. mesh Ewald, P. An N· log (N) method for Ewald sums in large systems. *J. Chem. Phys* **98**, 10089–10092 (1993).
104. Berendsen, H. J. C., Postma, J. P. M. van, van Gunsteren, W. F., DiNola, A. & Haak, J. R. Molecular dynamics with coupling to an external bath. *J Chem Phys* **81**, 3684–3690 (1984).
105. Bussi, G., Donadio, D. & Parrinello, M. Canonical sampling through velocity rescaling. *J Chem Phys* **126**, 014101 (2007).
106. Parrinello, M. & Rahman, A. Polymorphic transitions in single crystals: A new molecular dynamics method. *J Appl Phys* **52**, 7182–7190 (1981).
107. Brehm, M. & Kirchner, B. TRAVIS-a free analyzer and visualizer for Monte Carlo and molecular dynamics trajectories. Preprint at (2011).
108. Brehm, M., Thomas, M., Gehrke, S. & Kirchner, B. TRAVIS—A free analyzer for trajectories from molecular simulation. *J Chem Phys* **152**, 164105 (2020).
109. Bannwarth, C., Ehlert, S. & Grimme, S. GFN2-xTB—An accurate and broadly parametrized self-consistent tight-binding quantum chemical method with multipole electrostatics and density-dependent dispersion contributions. *J Chem Theory Comput* **15**, 1652–1671 (2019).
110. Neese, F. The ORCA program system. *Wiley Interdiscip Rev Comput Mol Sci* **2**, 73–78 (2012).
111. Roemelt, M., Maganas, D., DeBeer, S. & Neese, F. A combined DFT and restricted open-shell configuration interaction method including spin-orbit coupling: Application to transition metal L-edge X-ray absorption spectroscopy. *J Chem Phys* **138**, 204101 (2013).
112. Maganas, D. *et al.* First principles calculations of the structure and V L-edge X-ray absorption spectra of V 2 O 5 using local pair natural orbital coupled cluster theory and spin–orbit coupled configuration interaction approaches. *Physical Chemistry Chemical Physics* **15**, 7260–7276 (2013).
113. Axel, D. B. Density-functional thermochemistry. III. The role of exact exchange. *J Chem Phys* **98**, 5648–5652 (1993).
114. Lee, C., Yang, W. & Parr, R. G. Development of the Colle-Salvetti correlation-energy formula into a functional of the electron density. *Phys Rev B* **37**, 785 (1988).
115. Schäfer, A., Horn, H. & Ahlrichs, R. Fully optimized contracted Gaussian basis sets for atoms Li to Kr. *J Chem Phys* **97**, 2571–2577 (1992).
116. Weigend, F. & Ahlrichs, R. Balanced basis sets of split valence, triple zeta valence and quadruple zeta valence quality for H to Rn: Design and assessment of accuracy. *Physical Chemistry Chemical Physics* **7**, 3297–3305 (2005).
117. Kendall, R. A. & Früchtl, H. A. The impact of the resolution of the identity approximate integral method on modern ab initio algorithm development. *Theor Chem Acc* **97**, 158–163 (1997).
118. Feyereisen, M., Fitzgerald, G. & Komornicki, A. Use of approximate integrals in ab initio theory. An application in MP2 energy calculations. *Chem Phys Lett* **208**, 359–363 (1993).

119. Pantazis, D. A., Chen, X.-Y., Landis, C. R. & Neese, F. All-electron scalar relativistic basis sets for third-row transition metal atoms. *J Chem Theory Comput* **4**, 908–919 (2008).

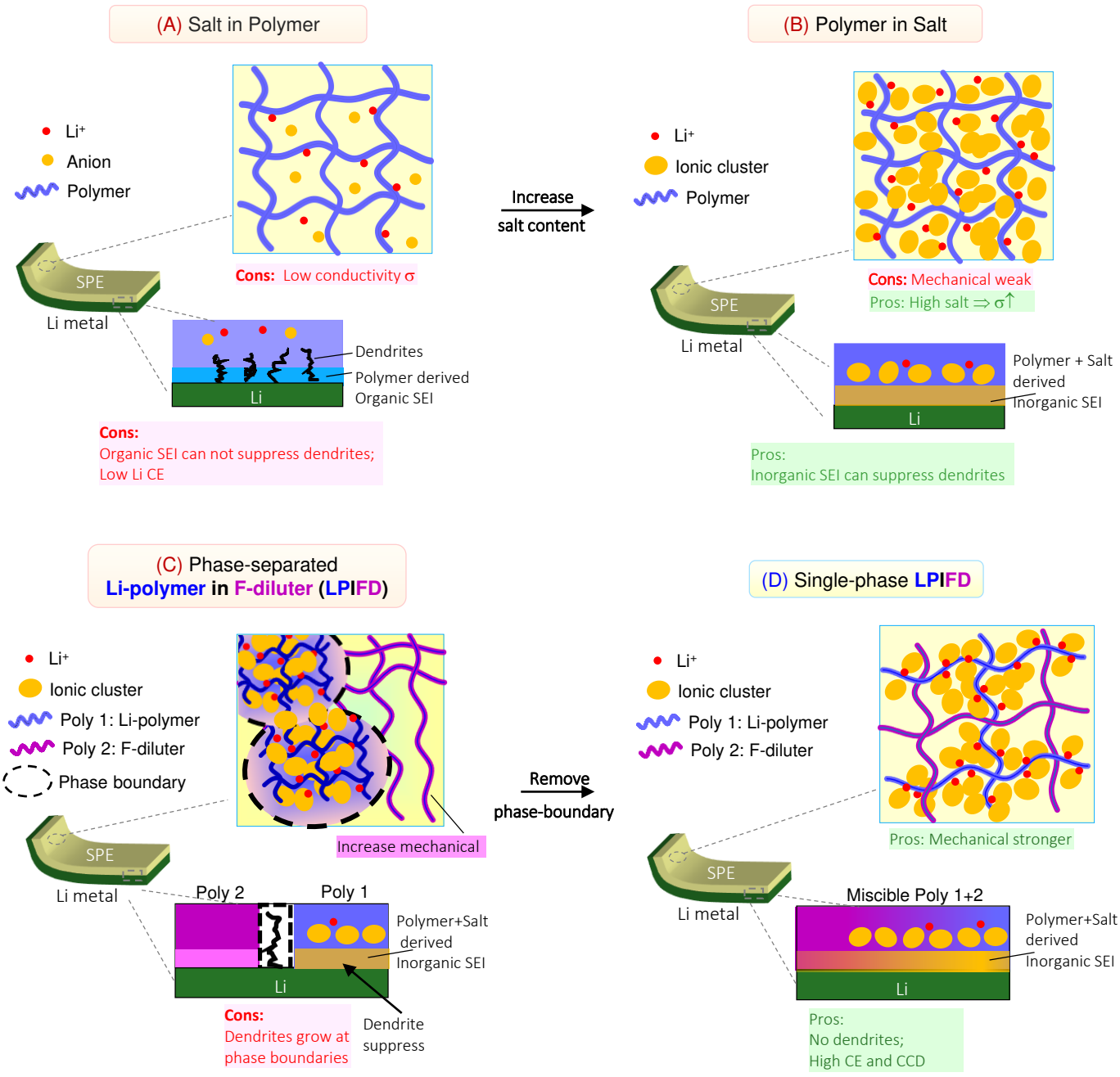
(A) Salt in Polymer
Li+
Anion
Polymer
SPE
Li metal
Cons: Low conductivity σ
Dendrites
Polymer derived
Organic SEI
Li
Cons:
Organic SEI can not suppress dendrites;
Low Li CE
Increase
salt content
(B) Polymer in Salt
Li+
Ionic cluster
Polymer
SPE
Li metal
Cons: Mechanical weak
Pros: High salt ⇒ σ↑
Polymer + Salt
derived
Inorganic SEI
Li
Pros:
Inorganic SEI can suppress dendrites
(C) Phase-separated
Li-polymer in F-diluter (LPIFD)
Li+
Ionic cluster
Poly 1: Li-polymer
Poly 2: F-diluter
Phase boundary
SPE
Li metal
Increase mechanical
Poly 2
Poly 1
Polymer+Salt
derived
Inorganic SEI
Li
Cons:
Dendrites grow at
phase boundaries
Dendrite
suppress
Remove
phase-boundary
(D) Single-phase LPIFD
Li+
Ionic cluster
Poly 1: Li-polymer
Poly 2: F-diluter
SPE
Li metal
Pros: Mechanical stronger
Miscible Poly 1+2
Polymer+Salt
derived
Inorganic SEI
Li
Pros:
No dendrites;
High CE and CCD

F-diluter: 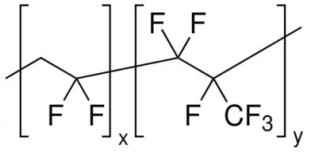 PVDF-HFP

①② **non-miscible with F-Diluter**

③-⑤, **miscible with F-diluter**

Li-polymer:

1 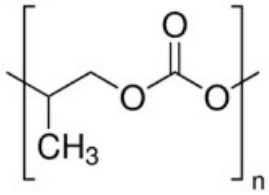

2 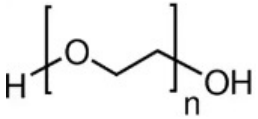

3 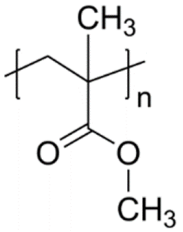

4 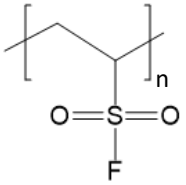

5 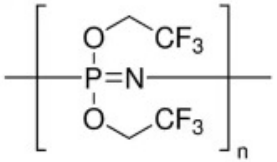

Organic-rich SEI → **Inorganic-rich SEI**

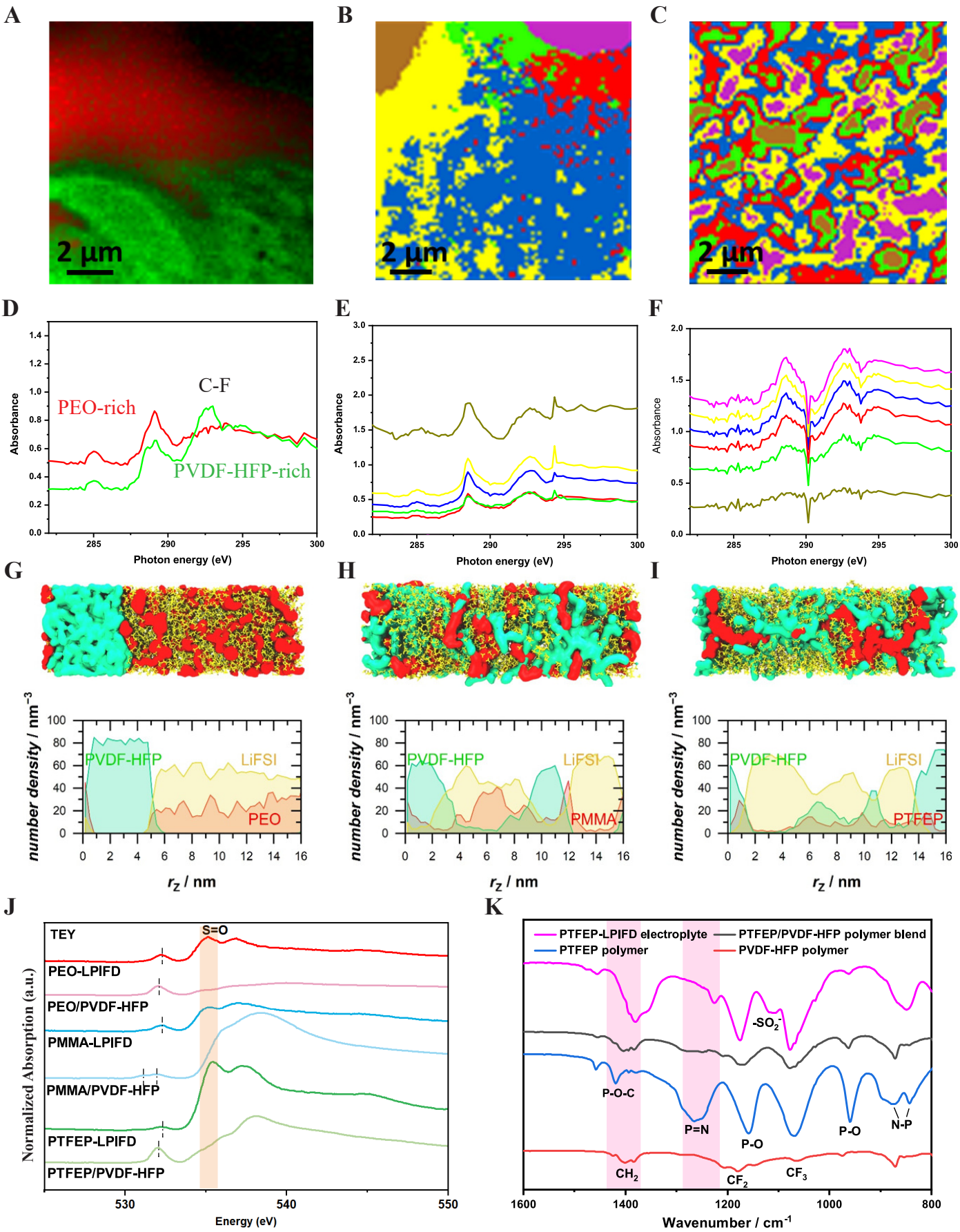
A
B
C
2 μm
2 μm
2 μm
D
E
F
Absorbance
PEO-rich
C-F
PVDF-HFP-rich
Photon energy (eV)
G
H
I
number density / nm^{-3}
PVDF-HFP
LiFSI
PEO
PMMA
PTFEP
r_z / nm
J
TEY
S=O
PEO-LPIFD
PEO/PVDF-HFP
PMMA-LPIFD
PMMA/PVDF-HFP
PTFEP-LPIFD
PTFEP/PVDF-HFP
Normalized Absorption (a.u.)
Energy (eV)
K
PTFEP-LPIFD electroplyte
PTFEP/PVDF-HFP polymer blend
PTFEP polymer
PVDF-HFP polymer
-SO$_2^-$
P-O-C
P=N
P-O
P-O
N-P
CH$_2$
CF$_2$
CF$_3$
Wavenumber / cm^{-1}

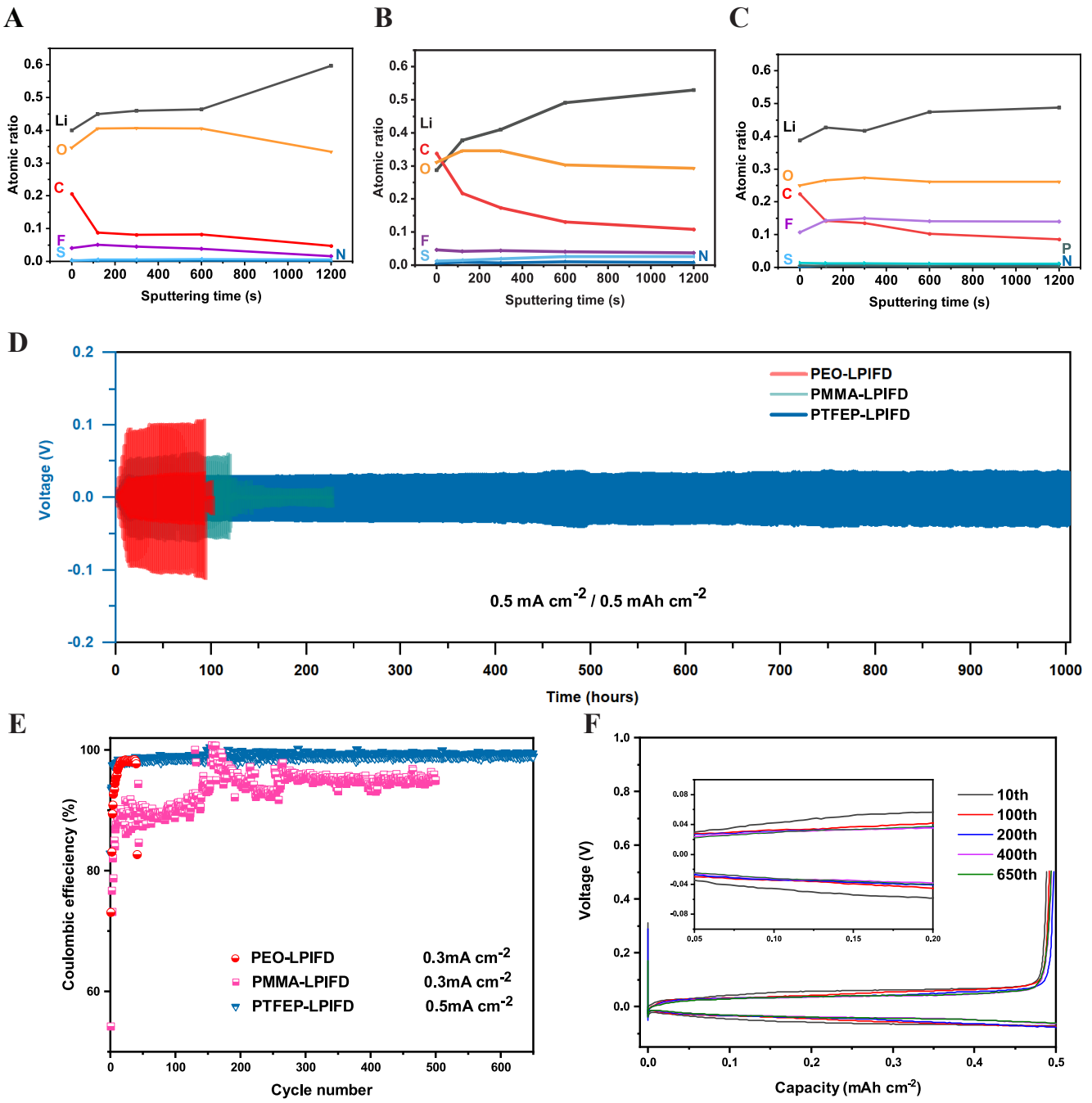
A
B
C
Atomic ratio
Sputtering time (s)
Li
O
C
F
S
N
P
D
Voltage (V)
Time (hours)
PEO-LPIFD
PMMA-LPIFD
PTFEP-LPIFD
0.5 mA cm-2 / 0.5 mAh cm-2
E
Coulombic effieciency (%)
Cycle number
PEO-LPIFD 0.3mA cm-2
PMMA-LPIFD 0.3mA cm-2
PTFEP-LPIFD 0.5mA cm-2
F
Voltage (V)
Capacity (mAh cm-2)
10th
100th
200th
400th
650th

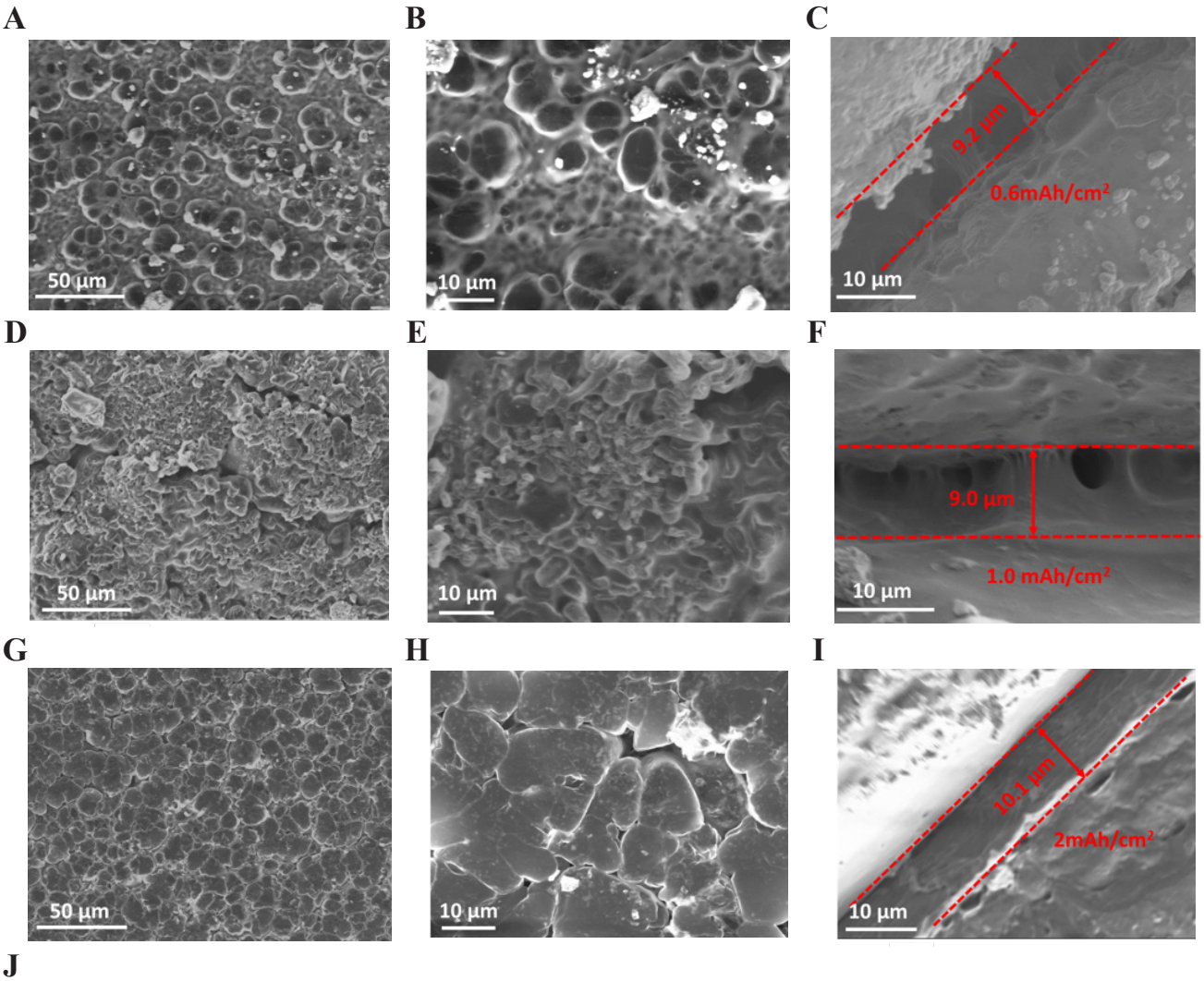

J

Li-polymer	#1 PPC	#2 PEO	#3 PMMA	#4 PVSF	#5 PTFEP
SEI	Organic-rich	Organic-less	Organic-rich	Organic-less	Organic-less, F-rich
Single-phase (LPIFD)	No	No	Yes	Yes	Yes
CCD	0.3	0.6	1.4	2.4	3.7
CE	<90%	~98	~95	~99	~99

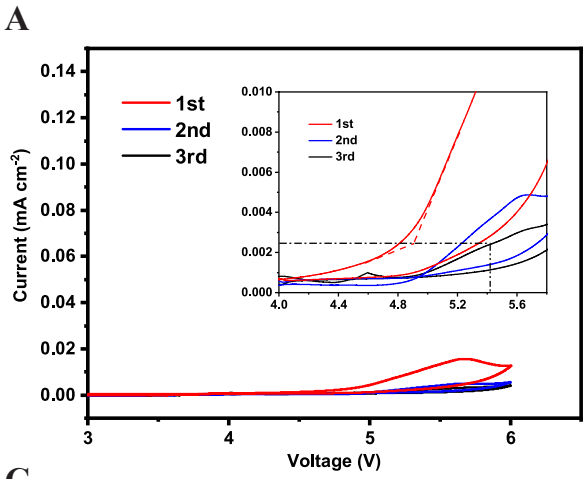
A
1st
2nd
3rd
Current (mA cm-2)
Voltage (V)

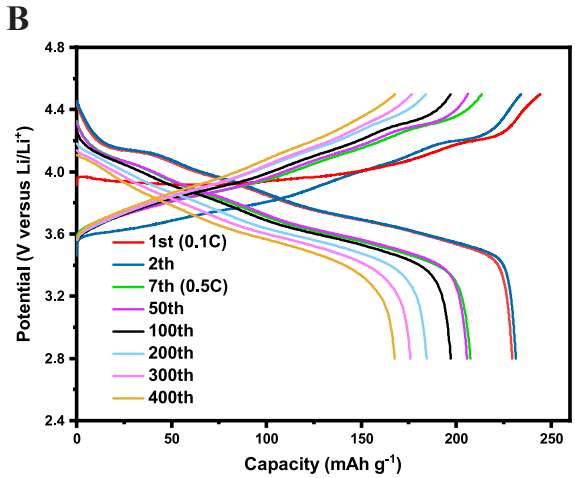
B
1st (0.1C)
2th
7th (0.5C)
50th
100th
200th
300th
400th
Potential (V versus Li/Li+)
Capacity (mAh g-1)

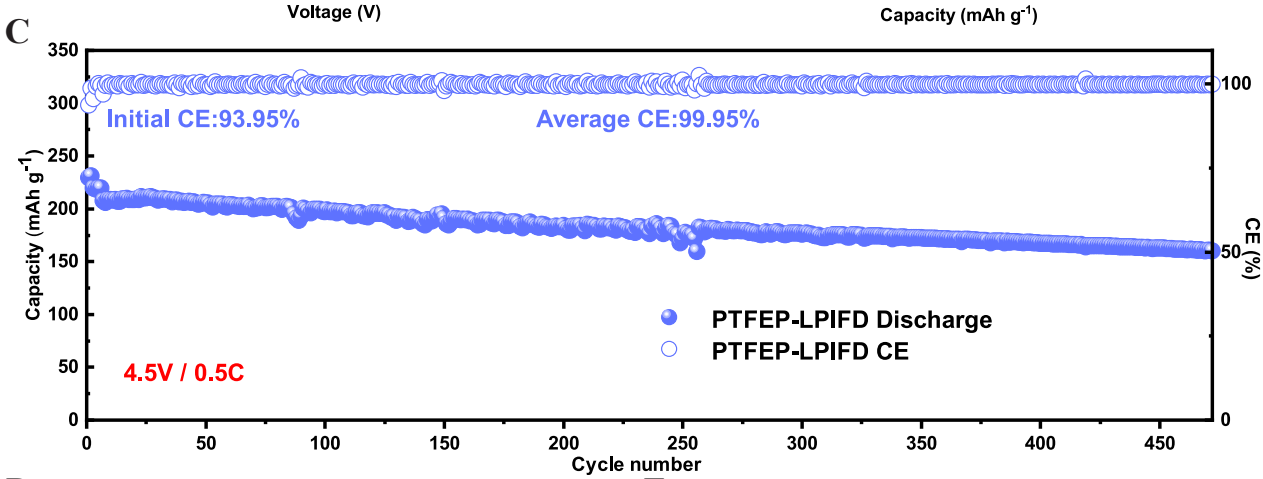
C
Initial CE:93.95%
Average CE:99.95%
PTFEP-LPIFD Discharge
PTFEP-LPIFD CE
4.5V / 0.5C
Capacity (mAh g-1)
CE (%)
Cycle number

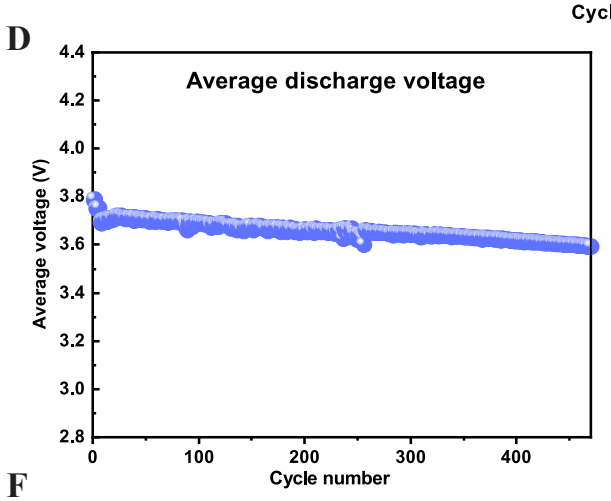
D
Average discharge voltage
Average voltage (V)
Cycle number

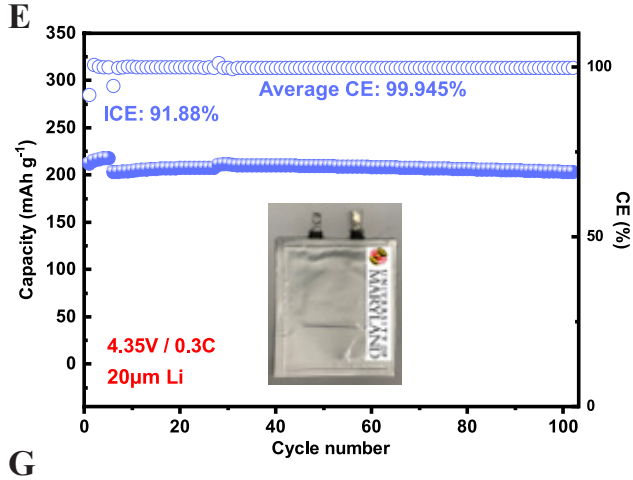
E
Average CE: 99.945%
ICE: 91.88%
4.35V / 0.3C
20μm Li
Capacity (mAh g-1)
CE (%)
Cycle number

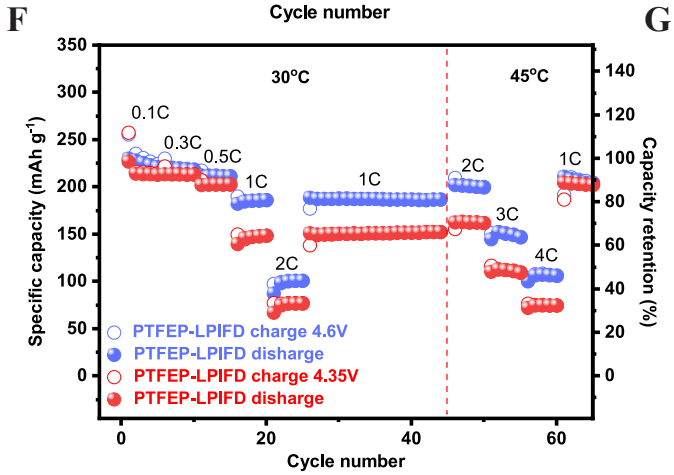
F
30°C
45°C
0.1C
0.3C
0.5C
1C
2C
1C
2C
3C
4C
1C
PTFEP-LPIFD charge 4.6V
PTFEP-LPIFD disharge
PTFEP-LPIFD charge 4.35V
PTFEP-LPIFD disharge
Specific capacity (mAh g-1)
Capacity retention (%)
Cycle number

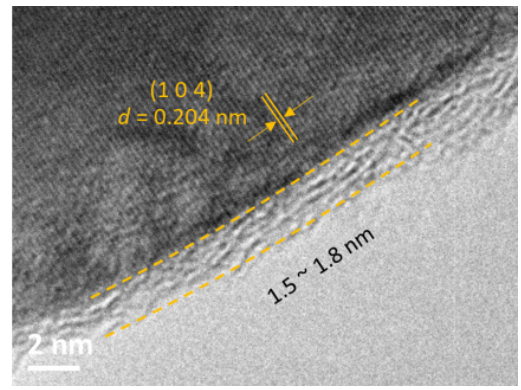
G
(1 0 4)
d = 0.204 nm
1.5 ~ 1.8 nm
2 nm